A&A, 708, A2 (2026)
https://doi.org/10.1051/0004-6361/202558695

Astronomy & Astrophysics

Driver behind the bimodal distribution of Eddington-scaled radio luminosity in nearby early-type galaxies

A. Wójtowicz[1,2,⋆], N. Werner[1], Ł. Stawarz[2], and C. C. Cheung[3]

[1] Department of Theoretical Physics and Astrophysics, Faculty of Science, Masaryk University, Kotlářská 2, Brno 61137, Czechia
[2] Astronomical Observatory, Jagiellonian University, ul. Orla 171, PL-30244 Kraków, Poland
[3] Space Science Division, Naval Research Laboratory, Washington, DC 20375, USA

Received 19 December 2025 / Accepted 4 February 2026

ABSTRACT

Context. Early-type galaxies host low-luminosity active galactic nuclei, as indicated by radio emission spanning up to several orders of magnitude in terms of the physical scale, ranging from compact parsec-scale to extended kiloparsec-scale radio morphology.

Aims. We investigate the Eddington-scaled radio luminosity distribution of nearby early-type galaxies in a large sample of 117 sources to confirm whether this distribution is bimodal, as previously inferred for a smaller sample of 62 galaxies. We also consider whether the bimodality can be attributed to specific host galaxy properties.

Methods. We compiled a sample of early-type galaxies with black hole masses measured using direct methods, as well as the radio flux densities at 1.4 GHz and 3 GHz. We used statistical tests to confirm whether the Eddington-scaled radio luminosities are bimodal. We investigated the properties of radio-dim and -bright sources, assessed the presence of extended jets with VLASS imaging, and examined host galaxy kinematics and central stellar structure.

Results. We confirm, using a twice larger sample of all known 1.4 GHz-detected early-type galaxies with directly measured black hole masses (117 galaxies), that the distribution of $L_{1.4\,\mathrm{GHz}}/L_{\mathrm{Edd}}$ is bimodal, with a characteristic antimode at $L_{1.4\,\mathrm{GHz}}/L_{\mathrm{Edd}} \approx -8.6$, which disappears when considering the subset of sources with black hole masses obtained using the $M_{\mathrm{BH}} - \sigma_{\star}$ relation. The radio-bright peak is dominated by galaxies hosting resolved jets, while radio-dim systems show compact nuclear emission with many showing excess radio emission relative to that expected from star formation as indicated by the well-known far-infrared and radio (FIR-radio) correlation. Moreover, we find that radio-bright galaxies are primarily slow rotators with depleted stellar cores, whereas radio-dim galaxies are predominantly fast rotators.

Conclusions. We show that nearby early-type galaxies with direct black hole mass measurements exhibit a clear bimodality in Eddington-scaled radio luminosity, separating radio-dim nuclei with compact emission from radio-bright systems hosting extended jets. The dichotomy correlates strongly with host-galaxy kinematics and central structure, suggesting that the ability to sustain jet production is governed primarily by galaxy assembly history and feeding mode, rather than by black hole mass or accretion rate alone. In this term, the radio output of radio-dim sources likely reflects modest, intermittent supplies of magnetized gas delivered to the accretion flow through stochastic processes and, most plausibly, the tidal disruption of giant-branch stars passing through the immediate vicinity of the supermassive black hole (SMBH).

Key words. catalogs – galaxies: active – galaxies: elliptical and lenticular, cD – galaxies: jets – galaxies: star formation

1. Introduction

Elliptical galaxies can be classified into two main groups based on their observed properties. One group consists of massive ellipticals, typically with stellar masses exceeding $\sim 10^{11}\,M_{\odot}$. These galaxies often possess halos of hot, X-ray–emitting gas and are frequently associated with strong radio sources (Bender et al. 1989). Their luminosity profiles commonly exhibit core flattening and boxy isophotes (Faber et al. 1997). Kinematic studies show that massive ellipticals usually rotate slowly and often contain kinetically decoupled components, while displaying a notable amount of rotation along the galaxy minor axis (Cappellari et al. 2007; Emsellem et al. 2007). On the other hand, less massive ellipticals rarely exhibit detectable X-ray halos and typically show weak or no radio emission. Their luminosity profiles generally follow a smooth, power law-like distribution and their isophotes tend to be more disk-like. Kinematically, these less massive galaxies often show significant rotation along the galaxy's major axis.

Elliptical galaxies are typical hosts of quasars, namely, active galactic nuclei (AGNs) accreting near the Eddington limit (e.g., Dunlop et al. 2003; McLure et al. 1999; Floyd et al. 2004). While all quasars, owing to the universality of accretion-disk emission, exhibit similar optical properties, their radio properties can vary substantially, with some quasars detected in the radio band, while others are not. A fundamental dichotomy in the underlying radio-emission mechanisms of quasars was first tentatively suggested in early studies by Kellermann et al. (1989), who proposed two distinct classes: radio-quiet and radio-loud quasars, based on the bimodal distribution of the ratio of radio-to-optical-flux densities.

Complementing this dichotomy among quasar sources and extending it to the broader population of elliptical galaxies exhibiting varying levels of nuclear activity, large-sky radio surveys show that radio-emitting galaxies fall into two broad morphological classes at the resolution typical of such surveys: (a) resolved systems with extended jets and (b) unresolved, compact radio sources.

The origin of radio emission in extended radio galaxies is relatively well established: their powerful outflows are thought

---

[⋆] Corresponding author: `awojtowicz@oa.uj.edu.pl`

to be launched via the Blandford–Znajek mechanism, where the rotational energy is extracted from a spinning black hole threaded by magnetic fields anchored in the surrounding accreting matter (Blandford & Znajek 1977). In this model, the outflow power is set by the mass supply (accretion rate), which regulates the magnetic flux threading the black hole horizon, and by the black hole spin. However, the physical mechanisms responsible for collimating and accelerating these outflows to their terminal bulk velocities remain a matter of debate.

The characteristics of radio emissions from compact radio galaxies continue to be somewhat enigmatic and shrouded in mystery. Radio emission, in principle, is mostly associated with synchrotron processes, where relativistic particles are accelerated in a turbulent magnetic field, preferentially at the fronts of strong shock waves. However, such conditions occur not only in AGN-driven winds or jets but also in star-forming regions, particularly in the central parts of galaxies, implying that both environments may contribute to the observed radio emission. A comprehensive summary of the problem associated with radio emission in various types of AGNs was presented in a number of studies, including reviews by Blandford et al. (2019) and Tadhunter (2016).

Observations of X-ray binaries support the importance of spin in launching the jet (Narayan & McClintock 2012); however, on the other hand, many active galaxies with measured high spin values are radio-quiet (see Reynolds 2021, for a recent review). Thus, it seems that high spin alone is not sufficient to launch powerful and collimated outflows, highlighting the importance of accretion rate and magnetic field accumulation. In most recent studies, particularly those based on numerical simulations (see Komissarov & Porth 2021, for a review), jets have indeed been found to form most efficiently in the "magnetically arrested disk" (MAD) regime. In this state, the poloidal magnetic flux accumulated near the black hole reaches saturation, enabling the efficient extraction of rotational energy from the ergosphere and creating a rigid, magnetically dominated funnel around the jet base that facilitates its initial collimation.

A comprehensive review of the radio emission mechanisms in radio-quiet AGNs is given in Panessa et al. (2019). Here, in this context and building on our previous analysis presented in Wójtowicz et al. (2023), we investigate the origin of the radio emission in a sample of early-type galaxies with accurately measured supermassive black-hole (SMBH) masses. These systems accrete at low or extremely low rates and are typically observed to be radio-faint.

In Wójtowicz et al. (2023), we used a sample of 62 early-type galaxies with directly estimated BH masses, $M_{\rm BH}$, to identify a possible bimodality in a distribution of the logarithm of the integrated 1.4 GHz radio luminosities. It is expressed as a fraction of their Eddington luminosities, $\log L_{1.4\,\rm GHz}/L_{\rm Edd}$, where $\log L_{\rm Edd}/{\rm erg\,s^{-1}} \simeq 38.1 + \log\, M_{\rm BH}/M_{\odot}$.

In this paper, we present a large sample of 123 early-type galaxies with significant radio detections at 1.4 GHz. Six sources were subsequently excluded because they only have upper limits to their BH mass estimates, thus giving a net sample of 117 galaxies for our analysis. We use this sample to test whether the bimodality identified in Wójtowicz et al. (2023) remains valid in the expanded sample.

2. Sample selection and data acquisition

An extensive search of the current literature allowed us to compile a list of all galaxies with central SMBH masses measured using direct methods, including measurements based on direct observations of gas and stellar kinematics, as well as from reverberation mapping. Here, we only focus and present the sample of early-type galaxies (i.e., lenticular or elliptical). These were classified through visual investigation of the available optical images in *Digital Sky Survey (DSS)*[1], *Sloan Digital Sky Survey (SDSS)*[2], and *Panoramic Survey Telescope & Rapid Response System (Pan-STARRS)*[3]. In cases of unclear morphology, we further investigated any available high-resolution images through *Hubble Legacy Archive*[4]. A galaxy was classified as early-type if its luminosity distribution decreased smoothly from the center and showed no signs of spiral arms or disturbance, such as tidal tails. Objects whose optical luminosity was dominated by the central QSO component were excluded, since the QSO light prevents reliable morphological classification.

The sample analyzed in Wójtowicz et al. (2023) only included sources that were previously examined in an X-ray studied sample by Gaspari et al. (2019), with the additional requirement of a 1.4 GHz detection and early-type morphology. In the present work, we relax this criterion by including all early-type galaxies listed in van den Bosch (2016) with reported 1.4 GHz fluxes. In their paper, van den Bosch (2016) compiled black hole mass measurements for a heterogenous sample of 294 galaxies, of which 141 have an early-type morphology. Among these, 34 either lack reported 1.4 GHz fluxes or have fluxes below the detection limit of the instrument. We included 16 additional sources that were not part of these earlier samples, for which more recent black hole mass estimates are available. We updated the masses of two further sources, namely, *PG 0026+129* and *NGC 7619*.

Figure 1 shows the distributions of black hole mass ($M_{\rm BH}$), distance (D), radio luminosity ($L_{1.4\,\rm GHz}$), and Eddington-scaled radio luminosity ($L_{1.4\,\rm GHz}/L_{\rm Edd}$). The top-right panel illustrates the selection effects on the $M_{\rm BH}$ distribution. In Wójtowicz et al. (2023), the requirement of an hot X-ray halo detection biased the sample towards higher black hole masses (white histogram) and smaller distances, compared to the underlying population of early-type galaxies from the van den Bosch (2016) parent catalog (green histogram) and the sample presented in this work (red histogram). However, the lower panels show that the ranges of $L_{1.4\,\rm GHz}$ and $L_{1.4\,\rm GHz}/L_{\rm Edd}$ covered by the samples are similar.

The full sample consists of 123 early-type galaxies. Six galaxies have only upper-limit estimates for their black hole masses (namely *UGC 1214, NGC 2685, NGC 3945, NGC 4382, UGC 9799*, and *NGC 4150*) and these have been excluded from the analysis presented in the subsequent sections of this paper. Most of these 123 sources were observed and detected with the NRAO Very Large Array (VLA) at 1.4 GHz with a 45 arcsec resolution, and cataloged in Condon et al. (1998). The corresponding integrated 1.4 GHz flux densities are also listed in the *NASA/IPAC Extragalactic Database (NED)*[5].

Flux densities for the faintest sources not included in the Condon et al. (1998) cataloged were taken from the Brown et al. (2011) study of a near-infrared-bright (NIR-bright; 2MASS $K <$ 9 mag) sample of early-type galaxies, where the estimates were derived from stacked NVSS images. Three additional sources (*NGC 1023, NGC 4429*, and *NGC 4459*) that were undetected in Brown et al. (2011) were later successfully detected in 1.4 GHz

---

[1] `https://archive.eso.org/dss/dss`

[2] `https://www.sdss.org/dr18/`

[3] `https://catalogs.mast.stsci.edu/panstarrs/`

[4] `https://hla.stsci.edu/`

[5] `https://ned.ipac.caltech.edu/`

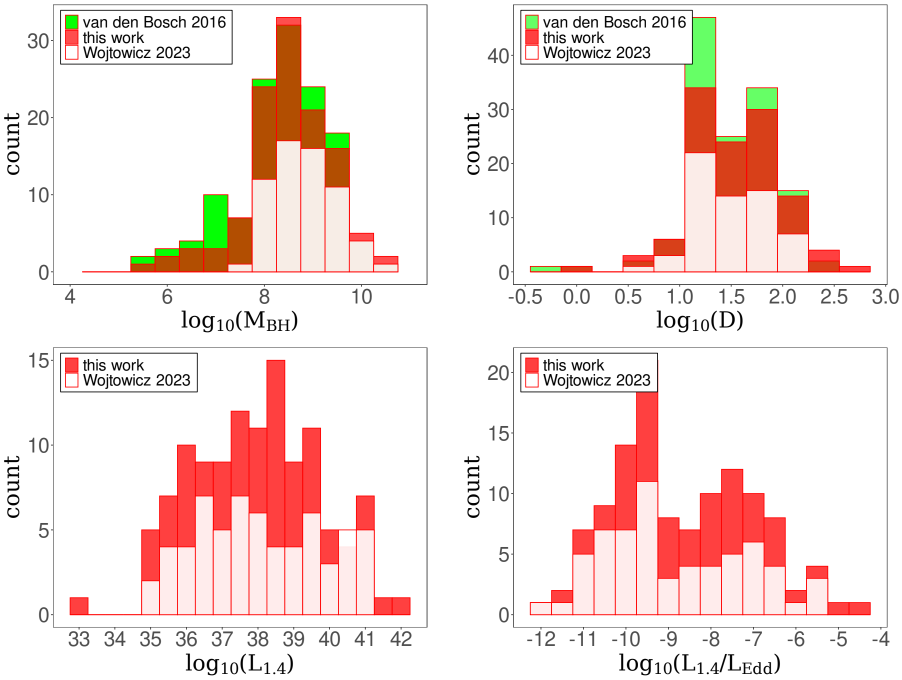

Fig. 1. Histogram showing the distribution of $\log_{10} M_{\rm BH}$ for sources presented in this work in red, Wójtowicz et al. (2023) in white, and early-type sources from van den Bosch (2016) in green in the top-right. Distribution of source distances (in Mpc), plotted on a logarithmic scale using the same color scheme in the top-left. The bottom-right and bottom-left histograms show the distributions of $\log_{10} L_{1.4}$ and $L_{1.4\,\rm GHz}/L_{\rm Edd}$ for sources from Wójtowicz et al. (2023) in white and this work in red, respectively.

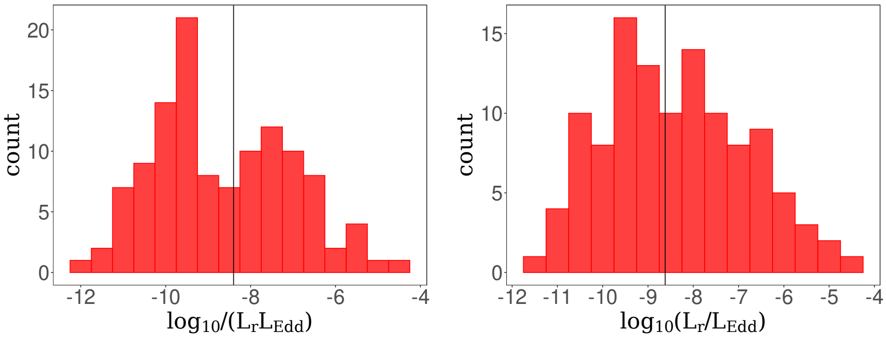

Fig. 2. Left: histogram of integrated 1.4 GHz radio luminosity expressed in Eddington units, estimated using BH masses determined via direct methods. The position of the antimode at $\log L_{1.4\,\rm GHz}/L_{\rm Edd} = -8.6$, identified using the locmodes function, is indicated by a black vertical line. Right: Same as the left panel, but using BH masses estimated indirectly from the $M_{\rm BH} - \sigma_*$ relation of Graham & Scott (2013). The vertical line indicates the position of the antimode at $\log L_{1.4\,\rm GHz}/L_{\rm Edd} = -8.6$.

VLA observations of early type galaxies from the *ATLAS*$^{\rm 3D}$ survey by Nyland et al. (2017).

For the brightest extended sources ($S_{1.4\,\rm GHz} > 0.6$ Jy), Brown et al. (2011) supplemented the 1.4 GHz VLA measurements from Condon et al. (1998) with low-resolution (≈12′) single-dish imaging from the 300-ft Green Bank and the 64-m Parkes radio telescopes in order to recover the total extended emission more accurately. Several of the brightest galaxies in our sample (*NGC 7626, NGC 0741, A 1836 BCG, NGC 3862, NGC 5128*) were later also re-examined by Allison et al. (2014) using archival 1.4 GHz NVSS data (Condon et al. 1998). They reported higher and more accurate flux densities than those listed in Brown et al. (2011) and we adopted the Allison et al. (2014) values for these objects. For two additional bright sources not included in the aforementioned catalogs, *Cygnus A* and *3C 390.3*, we used the fluxes reported in Bîrzan et al. (2004) and White & Becker (1992), respectively. The integrated 1.4 GHz radio luminosities of the studied galaxies span almost ten orders of magnitude, from $\sim 10^{32}$ to $\sim 10^{42}$ erg s^{-1}. Among these sources, 16 were detected at only a marginal significance (i.e., $S/N < 3$).

To complement these measurements, we also utilized 3 GHz VLASS data, which provide 2.5 arcsec resolution. The 8 arcsec cutout maps were obtained using the CIRADA server[6]. Radio maps were successfully retrieved for 121 of the 123 objects in our sample. Two sources, *NGC 5128* (located at $Dec < -43°$) and *Cygnus A* (which saturates the VLASS images), are not covered by the survey. Among the VLASS detections, 24 sources show no significant emission at the expected position, 48 exhibit only an unresolved radio core coincident with the host galaxy, and 10 show tentative evidence for small-scale extended structures. Table A.1 in Appendix A presents our full sample together with the measured radio fluxes and the corresponding references.

3. Radio emission of early-type galaxies

3.1. Integrated 1.4 GHz radio flux

In Figure 2, we show the histogram of $\log L_{1.4\,\rm GHz}/L_{\rm Edd}$ for all 117 sources with precise BH masses. The left panel presents the distribution based on BH masses estimated via one of the direct methods, while the right panel presents the corresponding distribution obtained indirectly from stellar velocity dispersion, using the scaling relation of Graham & Scott (2013). Notably, the bimodal structure evident in the direct-method distribution disappears when the BH masses are estimated using the scaling relation.

To robustly identify the true number of modes in our integrated $\log L_{1.4\,\rm GHz}/L_{\rm Edd}$ distribution, we fit the Gaussian mixture models with number of components ranging from one to five.

---

[6] `http://cutouts.cirada.ca/`

Table 1. Fitted components of Gaussian mixture model.

x	μ_1	μ_2	σ_1	σ_2	p	"VI"
$\log \frac{L_{1.4\,\mathrm{GHz}}}{L_{\mathrm{Edd}}}$	−9.88	−7.20	0.84	1.07	0.54	1.15

Notes. Gaussian mixture model given with function: $f(x) = p \times f_1 + (1 - p) \times f_2$, where $f_1 \sim N(\mu_1, \sigma_1)$ and $f_2 \sim N(\mu_2, \sigma_2)$ denote normal distributions, and p is the mixture weight. VI stands for "value indicated" in Table 2 of Schilling et al. (2002).

This method is implemented in the `GaussianMixtures` function in `sBIC` package in R-Studio Statistical Software. Based on this analysis and according to the singular Bayesian information criterion (sBIC) (Drton & Plummer 2017), we found that the two-mode Gaussian mixture model provides the best description of our data. Next, to further test the bimodal hypothesis, we used a maximum likelihood method implemented in the `mle2` function of `bbmle` package in R, to fit a mixture of two Gaussians $f(x) = p \times f_1 + (1 - p) \times f_2$, where f_1 and f_2 denote normal distributions, and p is the mixture weight. The parameters of the mixture distribution $f(x)$ obtained through the maximum likelihood method are shown in Table 1.

We applied the criterion of Schilling et al. (2002) stating that the mixture density, $f(x) = p \times f_1 + (1 - p) \times f_2$, is bimodal only if $|\mu_2 - \mu_1|$ exceeds $(\sigma_1 + \sigma_2)$ times the value indicated where the "value indicated" depends on the standard deviation ratio and the weight (see Table 2 therein). In our case, $\sigma_1/\sigma_2 \approx 0.78$ and $p \approx 0.5$, implying according to Schilling et al. (2002) that our mixture density is bimodal if and only if $|\mu_2 - \mu_1| > 1.25 \times (\sigma_1 + \sigma_2)$. This condition is satisfied for the values of the model parameters obtained using the maximum likelihood method as provided in Table 1. This supports the presence of the two modes in the analyzed dataset.

We find the position of the antimode in the $\log L_{1.4\,\mathrm{GHz}}/L_{\mathrm{Edd}}$ distribution using the R-Studio Statistical Software and locmodes function, implemented in the package multimode from the CRAN repository. We set the true number of modes, $mod0 = 2$, as supported by the analysis presented above. The position of the antimode was found at $\log L_{1.4\,\mathrm{GHz}}/L_{\mathrm{Edd}} = -8.6$ dividing our sample into two categories: "radio-dim" objects with $\log L_{1.4\,\mathrm{GHz}}/L_{\mathrm{Edd}} \leq -8.6$ and "radio-bright" if $\log L_{1.4\,\mathrm{GHz}}/L_{\mathrm{Edd}} > -8.6$. Here, we note that 34 early-type sources from van den Bosch (2016), which either lack reported 1.4 GHz flux measurements or have fluxes below the instrumental detection limit (0.5 mJy), are not included in this paper. These sources would be classified as radio-dim, with $\log(L_{1.4\,\mathrm{GHz}}/L_{\mathrm{Edd}}) \ll -8.6$.

3.2. VLASS radio core emission at 3 GHz

We investigated whether the distribution of 3 GHz core luminosity expressed as the fraction of Eddington luminosity, $\log L_{3\,\mathrm{GHz}}/L_{\mathrm{Edd}}$, is also bimodal. Thus, we utilized the 3 GHz VLASS radio maps to measure the fluxes associated with core emission; namely, we measured the fluxes from beam size area centered at the position of host galaxy coordinates. The fluxes were measured through the Analysis task in DS9 software following the Gaussian beam–area formula,

$$F = S \times \frac{\mathrm{PS}^2\, 4 \ln 2}{\pi\, \theta_{\mathrm{maj}}\, \theta_{\mathrm{min}}}, \qquad (1)$$

where F is the flux spectral density measured in Jy, S is the sum of pixel values provided in Jy/beam units, and PS is the pixel size in arscec^2, while θ_{maj} and θ_{min} are the beam FWHM axes measured in arsecs. The obtained core flux densities are given in Table A.1.

To investigate the true number of modes in the $\log L_{3\,\mathrm{GHz}}/L_{\mathrm{Edd}}$ distribution within our dataset, we performed an analogous analysis as that performed for the 1.4 GHz integrated radio luminosity. However, a fit of the Gaussian mixture models to the distribution of $\log(L_{3\,\mathrm{GHz}}/L_{\mathrm{Edd}})$, with the number of components ranging from one to five, strongly prefers a unimodal Gaussian distribution; thus, we found no evidence to support a bimodal distribution in core-related $\log(L_{3\,\mathrm{GHz}}/L_{\mathrm{Edd}})$.

4. IR diagnostics

4.1. WISE colours

WISE magnitudes for the analyzed sources were obtained by cross-matching the sample coordinates with the WISE All-Sky Survey catalog, adopting a matching radius of 12″. In Figure 3, we show the radio-faint and radio-bright sources separately on the WISE color-color diagnostic diagram. The corresponding photometric information is summarized in Table B.1, presented in Appendix B.

It is clear that the sample is not homogeneous in terms of nuclear activity. In particular, about 15 radio-bright galaxies show mid-IR (MIR) emission dominated by the AGN component, most likely associated with hot circumnuclear dust reprocessing the UV/X-ray radiation from accretion onto the SMBH (see, e.g., Jarrett et al. 2011; Stern et al. 2012; Mateos et al. 2012). Two radio-faint galaxies, NGC 1194 and NGC 5252, also stand out as notable outliers, with NGC 1194 exhibiting the most extreme $W1 - W2$ color in the sample. The remaining sources closely follow the tight "star formation sequence" introduced by Jarrett et al. (2019), which can be approximated by the functional form,

$$(\mathrm{W1} - \mathrm{W2}) = 0.015 \times e^{(\mathrm{W2}-\mathrm{W3})/1.38} - 0.08, \qquad (2)$$

indicated in Figure 3 by the dashed curve. Thus, basically all radio-faint sources, as well as the majority of the radio-bright ones, appear to be ISM-dominated in the IR regime. Consequently, the far-infrared (FIR) diagnostics discussed below for assessing the origin of the radio emission are robust, in the sense that they reliably identify the "radio-excess" systems.

We note that in this context that several of our radio-dim galaxies are characterized by $\mathrm{W1} - \mathrm{W2} < 0$, indicating that their NIR emission is dominated by stellar photospheres on the Rayleigh–Jeans tail, with essentially no detectable contribution from warm dust. Such colors place these systems below the star-formation sequence of Jarrett et al. (2019) and are characteristic of passive, dust-poor hosts with negligible star formation and no radiatively efficient AGN. In this regime, star formation cannot account for the observed radio emission and the lack of a MIR AGN signature likewise excludes the presence of a persistent accretion disk.

4.2. FIR-radio correlation

We compiled 60 μm and 100 μm FIR fluxes for all sources in our target list, except for 21 sources which lack any FIR measurements. This was achieved by matching the coordinates of our sources with *IRAS Point Source catalog v.2, Serendipitous Survey catalog* and *Faint Sources catalog*, adopting the matching

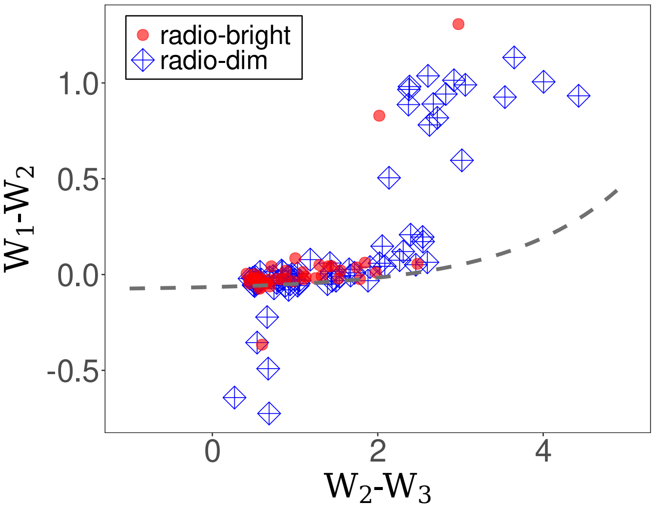

Fig. 3. WISE color-color diagram for the analyzed early-type galaxies. Sources belonging to the radio-dim and radio-bright classes are denoted as open blue diamonds and filled red circles respectively. The dashed line indicates the star formation sequence, as in Equation (2).

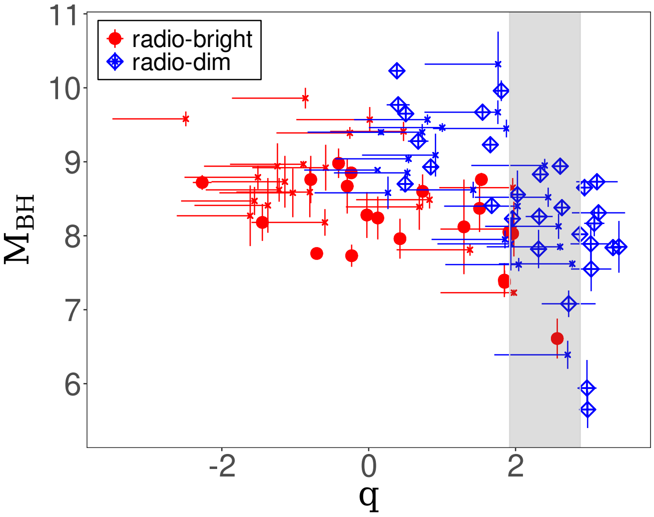

Fig. 4. FIR–radio correlation for the analyzed early-type galaxies. Symbols denote the same classes of sources as in Figure 3, except for objects with only upper limit measurements in the FIR, which are marked with stars. Gray shaded area denotes the q-values consistent with the range corresponding $q = 2.40 \pm 2\sigma_q$ with $\sigma_q = 0.24$ (Ivison et al. 2010).

radius 30 arcsec. If a source was detected in more than one catalog, we adopted the fluxes from our preferred catalog, following the priority order: Point Source Catalog, Faint Source Catalog, and, finally, Serendipitous Survey Catalog. For sources that are not identified in these catalogs, we explored NASA/IPAC Extragalactic Database[7] to check the availability of the fluxes at 60 µm and 100 µm measured in archival IRAS observations. The final list of the IR fluxes is given in Tables C.1 and C.2 in Appendix C.

The FIR–radio correlation is well established at all redshifts, with star-forming galaxies expected to lie within a narrow range of values of the q parameter defined by Helou et al. (1985) as

$$q \equiv \log \frac{F_{\rm FIR}/3.75\times10^{12}\,{\rm W\,m^{-2}}}{S_{1.4\,{\rm GHz}}/{\rm W\,m^{-2}\,Hz^{-1}}}, \tag{3}$$

where $F_{\rm FIR}/{\rm W\,m^{-2}} = 1.26\times10^{-14}\,[2.58\times S_{60\,\mu{\rm m}}/{\rm Jy}+S_{100\,\mu{\rm m}}/{\rm Jy}]$. In Figure 4, we plot the distribution of this FIR-radio colour in our sample as a function of the BH mass. As before, radio-bright sources with $\log L_{1.4\,{\rm GHz}}/L_{\rm Edd} > -8.6$ are denoted in the figure with red color and radio-dim sources with $\log L_{1.4\,{\rm GHz}}/L_{\rm Edd} < -8.6$ are marked with blue. The shaded areas in the plot denote the range corresponding to the median $q = 2.40$ with $\pm2\sigma_q$ dispersion, where $\sigma_q = 0.24$, as established by Ivison et al. (2010) for the galaxies in the GOODS-North field, based on the *Herschel* and VLA observations (also see in this context Magnelli et al. 2015; Delhaize et al. 2017; Giulietti et al. 2022).

It follows from the figure that all sources in the radio-bright sample are indeed over-luminous in the radio relative to their FIR and radio colors. A substantial fraction of the radio-dim sources however exhibit the same behavior, particularly those hosting black holes with masses $\log M_{\rm BH}/M_\odot \gtrsim 8.5$. Nevertheless, many radio-dim sources do fall within the star-forming region of the diagram, with some even showing unusually high q values.

5. Discussion

While radio-bright sources exhibit radio emission dominated by synchrotron radiation from a spatially resolved jet, radio-dim systems present a more ambiguous case. At the angular resolution of the 3 GHz VLASS observations (2.5 arcsec), the radio-dim sources remain unresolved. In Sect. 4.2, we showed that a subset of our sources exhibits FIR/radio ratios consistent with expectations for star-formation–dominated emission. However, a substantial fraction appears overluminous in the 1.4 GHz band, while remaining unresolved in higher resolution 3 GHz observations.

The physical mechanisms responsible for the compact, low-luminosity radio emission of radio-dim sources therefore remain unclear, suggesting in principle that both star formation and AGN-related processes might be contributing. In the following, we discuss the possible origin of the radio emission in our sample and what mechanisms may give rise to the bimodal distribution of radio luminosities.

5.1. Star-formation and radio emission

In general, early-type galaxies exhibit low star-formation rates, typically $\lesssim 0.1\,M_\odot\,{\rm yr}^{-1}$, due to the fact that they tend to be dust- and gas-poor. The most massive ellipticals can reach values of order $\sim 1\,M_\odot\,{\rm yr}^{-1}$ (Kokusho et al. 2017; Capetti et al. 2022). Even such modest levels of star formation can however produce monochromatic radio luminosities up to $\sim 10^{37}\,{\rm erg\,s^{-1}}$. Thus, especially in the low-luminosity radio regime $\lesssim 10^{37}\,{\rm erg\,s^{-1}}$, the contribution of electrons accelerated in star-forming regions to the total radio emission of early-type systems is never negligible.

Despite this low level of star formation overall, the spatial distribution and intensity of star-formation activity can be highly diverse in early-type systems depending on the exact amount of cold gas present in the ISM. It was shown, for example, by Shapiro et al. (2010) and Kuntschner et al. (2010), that enhanced star formation in nearby early-type galaxies is confined to fast rotators occurring in two distinct modes: (i) widespread young stellar populations associated with substantial molecular gas reservoirs and (ii) more compact star-forming structures arranged in disks or rings (see also Young 2002, 2005; Young et al. 2011). In some cases, the young stars are concentrated toward the central regions (Kuntschner et al. 2010).

---

[7] https://ned.ipac.caltech.edu/

More evidence on the dual nature of early-type galaxies follows from the analysis of broadband spectral energy distribution modeling with CIGALEMC code (Serra et al. 2011) by Amblard et al. (2014). Their results revealed a bimodal distribution in the specific star formation rates of early-type galaxies, with lenticular galaxies exhibiting, on average, higher specific star-formation rates and dust luminosities than classical elliptical galaxies. This suggests that residual star formation may be more common and extended in at least a subset of early-type systems, particularly those retaining disk-like structures and molecular gas.

We note that obtaining reliable star formation rates for the early-type galaxies in our sample is of particular importance in distinguishing the source of radio emission in these systems, particularly at the low-luminosity end. These results will be presented in a dedicated follow-up paper (in prep.).

In this context, the q-factor, defined as the FIR-to-radio luminosity ratio (see Equation (3)), provides valuable insight into the dominant contribution of young stars to the total radio emission of a galaxy. As discussed in Section 4.2, a large fraction of our radio-dim sources (in principle, almost all with SMBH masses of $\log M_{\rm BH}/M_{\odot} < 8.5$) exhibit q-factor values that are consistent with radio emission being indeed dominated by star-forming regions. However, a notable subset of radio-dim sources (in particular, all radio-dim systems with SMBH masses $\log M_{\rm BH}/M_{\odot} > 9.0$) shows evidence of radio excess, indicating the presence of an additional emission mechanism. Thus, despite the fact that there is compelling evidence for the bimodal nature of the star-formation rate in early-type galaxies, this alone cannot fully explain the observed bimodal distribution in $\log L_{1.4\,\rm GHz}/L_{\rm Edd}$; instead, it appears to be linked to the masses of the central SMBHs.

5.2. Role of star–SMBH interaction in triggering radio activity

Launching extended, powerful jets spanning more than hundreds of kiloparsecs (kpc), as observed in some sources, requires a sustained and long-lasting supply of matter to the accretion flow. On the other hand, if the matter supply is more sporadic and arrives in small parcels, the jets will not develop large-scale structures and will instead remain confined to the host galaxy environment.

Indeed, such a mechanism was proposed by Readhead et al. (2024) and further developed by Sullivan et al. (2024) to explain the emission properties of radio galaxies belonging to the compact symmetric object (CSO) class. These systems show a sharp cutoff in the distribution of the linear sizes of their radio structures at ~500 pc (Kiehlmann et al. 2024a,b), as well as high separation velocities of their terminal hotspots that imply short jet lifetimes. It has been proposed that the radio jets in such sources may be triggered by a single tidal disruption event (TDE); for example, the disruption of a giant-branch star in the vicinity of the central supermassive black hole.

As argued by Sullivan et al. (2024, see Section 5 therein), if the disrupted star carries an average magnetic field of $\gtrsim$100 G and passes only within ~100 gravitational radii from a SMBH, the event could still supply sufficient magnetic flux to seed jet formation and power outflows with luminosities on the order of $\sim 10^{33}\,{\rm erg\,s^{-1}}$ via the Blandford & Znajek (1977) mechanism. The subsequent evolution of the infalling debris could possibly further amplify the magnetic field near the SMBH, providing additional fuel supply capable of powering even the most luminous CSO sources. In our case, we are considering radio-dim systems unresolved at radio frequencies (on arcsecond scales), with black-hole masses of $M_{\rm BH} \sim (10^9 - 10^{10})\,M_{\odot}$ and integrated 1.4-GHz luminosities of $L_{1.4\,\rm GHz} \sim (10^{-12} - 10^{-9})\,L_{\rm Edd} \sim 10^{35} - 10^{39}\,{\rm erg\,s^{-1}}$, which are far below the radio luminosities of the classic CSOs discussed by Readhead et al. (2024) and Sullivan et al. (2024), along with q parameters indicating radio emission in excess of that expected from ongoing star formation. We find that the required energetic output is modest enough to be supplied by such TDE-driven, short-lived jet episodes.

Table 2. Summary of Bayesian linear regression analysis for radio-dim and -bright subsamples.

Sub-sample	a	b	$\sigma_{\rm int}$
Radio-dim	8.57 ± 0.06	4.79 ± 0.38	0.43 ± 0.05
Radio-bright	8.31 ± 0.07	$4.29^{+0.46}_{-0.43}$	$0.38^{+0.06}_{-0.05}$

5.3. Merger history of host galaxies

Some information on the merger history of the host galaxy can be assessed via an analysis of their (starlight) luminosity profiles. In particular, some luminous early-type galaxies exhibit partially depleted stellar cores, observed as a flattening of the luminosity profile in the inner region (Graham et al. 2003). A widely favored explanation for this feature involves the presence of a supermassive binary black hole, which ejects stars into radial orbits via three-body interactions (Begelman et al. 1980; Ebisuzaki et al. 1991; Quinlan 1996; Yu 2002; Merritt & Milosavljević 2005). In our sample, only 12 of the 35 radio-dim galaxies with well-characterized luminosity profiles show evidence of core depletion, while 7 of 11 radio-bright galaxies with studied luminosity profiles possess depleted cores (see Savorgnan et al. 2016; Davis et al. 2019; Sahu et al. 2019a).

Another valuable piece of information on the violent past of some early-type galaxies can also be obtained from their internal kinematics. The ATLAS$^{\rm 3D}$ survey of a volume-limited sample of local early-type galaxies found that most of them exhibit significant rotation along their major axes (Cappellari et al. 2011a,b; Emsellem et al. 2011; Krajnović et al. 2011). Of the 35 galaxies from our sample included in ATLAS$^{\rm 3D}$, 29 are radio-dim and only 6 are radio-bright. Among the radio-bright subsample, 50% of the galaxies are classified as fast rotators, while 22 out of 29 radio-dim galaxies (76%) fall into this category.

Although radio-bright sources are generally underrepresented in such surveys, these statistics suggest that radio-dim galaxies are preferentially associated with fast-rotating systems. Thus, they are more likely to lack depleted cores, pointing to their less violent merger history.

5.4. $M_{\rm BH} - \sigma_*$ scaling relation

The observed strong correlation between dynamically measured black hole masses, $M_{\rm BH}$, and the stellar velocity dispersion within the effective radius of host galaxies, σ_*, is considered to be a clear manifestation of the co-evolution of central SMBHs and their hosts. Since its discovery (Gebhardt et al. 2000; Ferrarese & Merritt 2000), significant efforts have been devoted to calibrating and understanding this correlation (e.g., van den Bosch 2016; Sahu et al. 2019a; Baldassare et al. 2020).

Recently, Smethurst et al. (2024) used the output from the Horizon-AGN simulation to show that galaxies experiencing more than three mergers since a redshift of $z = 2$ exhibit a

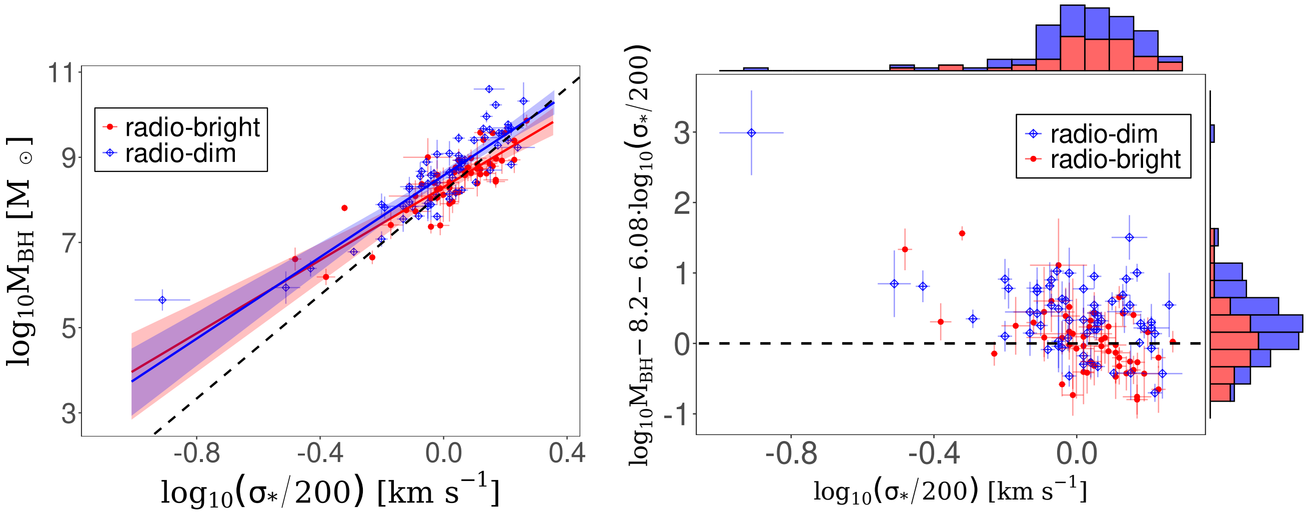

Fig. 5. Left panel: Relation between black hole mass ($\log_{10} M_{\rm BH}$) and stellar velocity dispersion ($\log_{10}(\sigma_*/200\,{\rm km\,s^{-1}})$) for the early-type galaxies in our sample. Radio-dim sources are shown as blue diamonds and radio-bright sources as red circles and their corresponding regression lines plotted as solid lines with shaded areas indicating 95% credibility intervals. The black dashed line shows the regression obtained by Graham & Scott (2013) for their full sample of 77 galaxies. Right panel: Scatter of the radio-dim and radio-bright sources from the mean regression line obtained by Graham & Scott (2013) as a function of velocity dispersion. The projected histograms of the source distributions along both axes are presented with the same color scheme for the two radio sub-types.

shallower correlation slope, whereas isolated galaxies are less tightly correlated and on average have steeper slopes. Similarly, Beckmann et al. (2023) reported that galaxies undergoing recent mergers tend to have lower spin values compared with those evolving in isolation.

Motivated by these findings, we examined the role of mergers and BH spin in shaping the observed radio-dim and radio-bright bimodality by analyzing the slopes of the respective $M_{\rm BH} - \sigma_*$ correlations. In Figure 5, we plot the $M_{\rm BH} - \sigma_*$ relation for our sample of early-type galaxies separated by radio-dim (blue) and radio-bright (red). Interestingly, the bimodality in our dataset is also reflected in the slightly different correlations of the two classes of objects in the $M_{\rm BH} - \sigma_*$ diagram. To quantify this difference, we performed a univariate linear regression analysis using the APEMoST algorithm[8] (Gruberbauer et al. 2009), with the response variable $Y = \log_{10} M_{\rm BH}$ and the predictor variable $X = \log_{10}(\sigma_\star/200\,{\rm km\,s^{-1}})$. We assumed a linear trend of

$$Y = a + b \cdot X + \epsilon, \tag{4}$$

where the noise term ϵ is normally distributed, $\epsilon \sim \mathcal{N}(0, \sigma)$. The standard deviation of the noise is expressed as

$$\sigma = \sqrt{\sum_{i=1}^{N} \sigma_{\rm int}^2 + \sigma_{Y_i}^2 + (b, \sigma_{X_i})^2}\,, \tag{5}$$

with $N = 46$ and $N = 71$ for the radio-bright and radio-dim samples, respectively. Here, $\sigma_{\rm int}$ represents the intrinsic scatter, while σ_{X_i} and σ_{Y_i} denote the respective measurement uncertainties associated with X_i and Y_i. The aim here is to determine the multidimensional probability density function (PDF) of the parameter set $\theta = a, b, \sigma_{\rm int}$.

Following Ostorero et al. (2017) and Wójtowicz et al. (2021), we performed 2×10^6 MCMC iterations with 20 chains to ensure a robust sampling of the parameter space. The resulting regression parameters are presented in Table 2.

Our analysis offers hints that the radio-dim and radio-bright sources might occupy different loci on the $M_{\rm BH}$–σ_* plane, although the substantial scatter within each subset limits the statistical significance. What we do see, in particular, is that radio-bright objects from our sample follow a shallower correlation than the one observed in radio-dim objects. Looking at the right panel of Figure 5, we see that (to first order) the radio-bright galaxies follow the mean $M_{\rm BH}$–σ_* relation of Graham & Scott (2013), whereas the radio-dim sources tend to lie slightly above that scaling. This suggests that the SMBHs in the radio-dim systems are, on average, overmassive relative to the stellar velocity dispersion of their hosts, compared to the general galaxy population used by Graham & Scott (2013).

For context, the Graham & Scott (2013) relation is based on a sample of 77 nearby galaxies with reliably measured SMBH masses and host-galaxy velocity dispersions. Their best-fitting power-law slope for this full sample, as well as for a refined subsample of 72 galaxies comprising 24 core-Sersic and 48 Sersic spheroids, is $b = 6.08 \pm 0.41$ and 6.08 ± 0.31, respectively. The sample spans a wide range of morphological types, including ellipticals, lenticulars, and spiral bulges, making it a broadly representative reference set for "normal" galaxies.

It is interesting to note in this context the recent findings of Gliozzi et al. (2024), who reported that AGNs in their sample produce a shallower $M_{\rm BH}$–σ_* correlation than that obtained for quiescent galaxies (Kormendy & Ho 2013). A similar behavior is seen in our dataset: the radio-dim galaxies presented in this paper yield a steeper correlation than the mean regression line of Graham & Scott (2013), whereas the radio-bright objects produce a comparatively shallower slope.

6. Conclusions

We investigated the distribution of Eddington-scaled radio luminosities among 117 nearby early-type galaxies with directly measured black hole masses. Using integrated 1.4 GHz flux densities and a sample that was approximately twice as large as that analyzed in Wójtowicz et al. (2023), we confirm a

---

[8] Automated Parameter Estimation and Model Selection Toolkit; `http://apemost.sourceforge.net/`, 2011 February.

bimodality in the $L_{1.4\,\mathrm{GHz}}/L_{\mathrm{Edd}}$ distribution, with peaks separated at $\log(L_{1.4\,\mathrm{GHz}}/L_{\mathrm{Edd}}) \approx -8.6$, dividing our sample into radio-dim ($\log(L_{1.4\,\mathrm{GHz}}/L_{\mathrm{Edd}}) \leq -8.6$) and radio-bright ($\log(L_{1.4\,\mathrm{GHz}}/L_{\mathrm{Edd}}) > -8.6$) objects. However, this structure is only recovered when using dynamical black hole masses and is washed out when masses from the $M_{\mathrm{BH}}-\sigma_{\star}$ relation are adopted or only a 3 GHz core luminosity is included.

High-resolution VLASS 3 GHz imaging shows that the radio-bright subset consists almost exclusively of galaxies hosting spatially extended jets, while radio-dim systems typically display compact nuclear emission. Many radio-dim galaxies, in particular those associated with the most massive black holes, still exhibit a radio excess relative to the FIR–radio correlation, indicating that the radio emission cannot be produced solely by star-forming processes, but must instead be dominated by mechanisms associated with SMBH activity.

The two radio populations appear to differ in their host-galaxy structural properties: the radio-bright systems are predominantly slow rotators with depleted stellar cores, whereas the radio-dim systems are mostly fast rotators. This distinction is further supported by their separation on the M_{BH}–σ_* plane, where the radio-dim sources exhibit a steeper regression slope than that obtained for the radio-bright objects. Moreover, when compared with the general population of normal galaxies of various morphological types studied by Graham & Scott (2013), the radio-dim systems appear, on average, to host overmassive SMBHs relative to their stellar velocity dispersions.

In our view, this points toward a scenario in which the radio-dim systems represent the low-energy tail of the radio-luminosity distribution normalized by SMBH mass in early-type galaxies. Their radio output likely reflects modest, intermittent supplies of magnetized gas delivered to the accretion flow through stochastic processes, most plausibly the tidal disruption of giant-branch stars passing through the immediate vicinity of the SMBH. Because the mass supply in such events is relatively uniform, the resulting accretion episodes produce broadly similar levels of radio emission across early-type systems. The observed bimodality in the Eddington-normalized radio-luminosity distribution would then arise primarily from the fact that a subset of fast rotators host overmassive black holes.

If correct, this scenario offers a coherent physical explanation for the bimodality in Eddington-normalized radio power at the lowest, rarely probed luminosity range in early-type galaxies. It would link SMBH radio output to stellar kinematic class and black-hole overmassiveness, while identifying stochastic stellar-disruption events as a universal fueling channel for low-level radio activity in these systems.

Acknowledgements. A. W. and N. W. were supported by the GACR grant 21-13491X. Research by C. C. C. at the Naval Research Laboratory is supported by NASA DPR S-15633-Y.

References

Allison, J. R., Sadler, E. M., & Meekin, A. M. 2014, MNRAS, 440, 696
Amblard, A., Riguccini, L., Temi, P., et al. 2014, ApJ, 783, 135
Baldassare, V. F., Dickey, C., Geha, M., et al. 2020, ApJ, 898, L3
Beckmann, R. S., Dubois, Y., Volonteri, M., et al. 2023, MNRAS, 523, 5610
Begelman, M. C., Blandford, R. D., & Rees, M. J. 1980, Nature, 287, 307
Bender, R., Surma, P., Doebereiner, S., et al. 1989, A&A, 217, 35
Bentz, M. C., & Manne-Nicholas, E. 2018, ApJ, 864, 146
Bîrzan, L., Rafferty, D. A., McNamara, B. R., et al. 2004, ApJ, 607, 800
Blandford, R. D., & Znajek, R. L. 1977, MNRAS, 179, 433
Blandford, R., Meier, D., & Readhead, A. 2019, ARA&A, 57, 467
Brough, S., Proctor, R., Forbes, D. A., et al. 2007, MNRAS, 378, 1507
Brown, M. J. I., Jannuzi, B. T., Floyd, D. J. E., et al. 2011, ApJ, 731, L41
Capetti, A., Brienza, M., Balmaverde, B., et al. 2022, A&A, 660, A93
Cappellari, M., Emsellem, E., Bacon, R., et al. 2007, MNRAS, 379, 418
Cappellari, M., Emsellem, E., Krajnović, D., et al. 2011a, MNRAS, 413, 813
Cappellari, M., Emsellem, E., Krajnović, D., et al. 2011b, MNRAS, 416, 1680
Condon, J. J., Cotton, W. D., Greisen, E. W., et al. 1998, AJ, 115, 1693
Condon, J. J., Cotton, W. D., & Broderick, J. J. 2002, AJ, 124, 675
Cooper, B. F. C., Price, R. M., & Cole, D. J. 1965, Aust. J. Phys., 18, 589
Dasyra, K. M., Tacconi, L. J., Davies, R. I., et al. 2007, ApJ, 657, 102
Davis, B. L., Graham, A. W., & Cameron, E. 2019, ApJ, 873, 85
Delhaize, J., Smolčić, V., Delvecchio, I., et al. 2017, A&A, 602, A4
den Brok, M., Krajnović, D., Emsellem, E., et al. 2021, MNRAS, 508, 4786
Diniz, S. I. F., Pastoriza, M. G., Hernandez-Jimenez, J. A., et al. 2017, MNRAS, 470, 1703
Drton, M., & Plummer, M. 2017, J. R. Stat. Soc. B, 79, 2
Dunlop, J. S., McLure, R. J., Kukula, M. J., et al. 2003, MNRAS, 340, 1095
Ebisuzaki, T., Makino, J., & Okumura, S. K. 1991, Nature, 354, 212
Emsellem, E., Cappellari, M., Krajnović, D., et al. 2007, MNRAS, 379, 401
Emsellem, E., Cappellari, M., Krajnović, D., et al. 2011, MNRAS, 414, 888
Faber, S. M., Tremaine, S., Ajhar, E. A., et al. 1997, AJ, 114, 1771
Ferrarese, L., & Merritt, D. 2000, ApJ, 539, L9
Floyd, D. J. E., Kukula, M. J., Dunlop, J. S., et al. 2004, MNRAS, 355, 196
Gaspari, M., Eckert, D., Ettori, S., et al. 2019, ApJ, 884, 169
Gebhardt, K., Bender, R., Bower, G., et al. 2000, ApJ, 539, L13
Giulietti, M., Massardi, M., Lapi, A., et al. 2022, MNRAS, 511, 1408
Gliozzi, M., Williams, J. K., Akylas, A., et al. 2024, MNRAS, 528, 3417
Golombek, D., Miley, G. K., & Neugebauer, G. 1988, AJ, 95, 26
Graham, A. W., & Scott, N. 2013, ApJ, 764, 151
Graham, A. W., Erwin, P., Trujillo, I., et al. 2003, AJ, 125, 2951
Gruberbauer, M., Kallinger, T., Weiss, W. W., et al. 2009, A&A, 506, 1043
Helou, G., Soifer, B. T., & Rowan-Robinson, M. 1985, ApJ, 298, L7
Ivison, R. J., Magnelli, B., Ibar, E., et al. 2010, A&A, 518, L31
Jarrett, T. H., Cohen, M., Masci, F., et al. 2011, ApJ, 735, 112
Jarrett, T. H., Cluver, M. E., Brown, M. J. I., et al. 2019, ApJS, 245, 25
Kabasares, K. M., Barth, A. J., Buote, D. A., et al. 2022, ApJ, 934, 162
Kellermann, K. I., Sramek, R., Schmidt, M., et al. 1989, AJ, 98, 1195
Kiehlmann, S., Lister, M. L., Readhead, A. C. S., et al. 2024a, ApJ, 961, 240
Kiehlmann, S., Readhead, A. C. S., O'Neill, S., et al. 2024b, ApJ, 961, 241
Knapp, G. R., Guhathakurta, P., Kim, D.-W., et al. 1989, ApJS, 70, 329
Kokusho, T., Kaneda, H., Bureau, M., et al. 2017, A&A, 605, A74
Komissarov, S., & Porth, O. 2021, New Astron. Rev., 92, 101610
Kormendy, J., & Ho, L. C. 2013, ARA&A, 51, 511
Krajnović, D., Emsellem, E., Cappellari, M., et al. 2011, MNRAS, 414, 2923
Kuntschner, H., Lucey, J. R., Smith, R. J., et al. 2001, MNRAS, 323, 615
Kuntschner, H., Emsellem, E., Bacon, R., et al. 2010, MNRAS, 408, 97
Liepold, C. M., Quenneville, M. E., Ma, C.-P., et al. 2020, ApJ, 891, 4
Magnelli, B., Ivison, R. J., Lutz, D., et al. 2015, A&A, 573, A45
Mateos, S., Alonso-Herrero, A., Carrera, F. J., et al. 2012, MNRAS, 426, 3271
McLure, R. J., Kukula, M. J., Dunlop, J. S., et al. 1999, MNRAS, 308, 377
Mehrgan, K., Thomas, J., Saglia, R., et al. 2019, ApJ, 887, 195
Merritt, D., & Milosavljević, M. 2005, Liv. Rev. Relat., 8, 8
Moshir, M., Kopan, G., Conrow, T., et al. 2008, VizieR Online Data Catalog: II/275
Narayan, R., & McClintock, J. E. 2012, MNRAS, 419, L69
Nyland, K., Young, L. M., Wrobel, J. M., et al. 2017, MNRAS, 464, 1029
Ostorero, L., Morganti, R., Diaferio, A., et al. 2017, ApJ, 849, 34
Panessa, F., Baldi, R. D., Laor, A., et al. 2019, Nat. Astron., 3, 387
Pilawa, J. D., Liepold, C. M., Delgado Andrade, S. C., et al. 2022, ApJ, 928, 178
Quinlan, G. D. 1996, New Astron., 1, 35
Readhead, A. C. S., Ravi, V., Blandford, R. D., et al. 2024, ApJ, 961, 242
Reynolds, C. S. 2021, ARA&A, 59, 117
Ricci, T. V., & Steiner, J. E. 2020, MNRAS, 495, 2620
Ricci, T. V., Steiner, J. E., & Menezes, R. B. 2016, MNRAS, 463, 3860
Rice, W., Lonsdale, C. J., Soifer, B. T., et al. 1988, ApJS, 68, 91
Saglia, R. P., Opitsch, M., Erwin, P., et al. 2016, ApJ, 818, 47
Sahu, N., Graham, A. W., & Davis, B. L. 2019a, ApJ, 876, 155
Sahu, N., Graham, A. W., & Davis, B. L. 2019b, ApJ, 887, 10
Sanders, D. B., Phinney, E. S., Neugebauer, G., et al. 1989, ApJ, 347, 29
Savorgnan, G. A. D., Graham, A. W., Marconi, A., et al. 2016, ApJ, 817, 21
Schilling, M., Watkins, A., & Watkins, W. 2002, Am. Stat., 56, 223
Serra, P., Amblard, A., Temi, P., et al. 2011, ApJ, 740, 22
Shapiro, K. L., Falcón-Barroso, J., van de Ven, G., et al. 2010, MNRAS, 402, 2140
Smethurst, R. J., Beckmann, R. S., Simmons, B. D., et al. 2024, MNRAS, 527, 10855
Stern, D., Assef, R. J., Benford, D. J., et al. 2012, ApJ, 753, 30
Sullivan, A. G., Blandford, R. D., Begelman, M. C., et al. 2024, MNRAS, 528, 6302
Tadhunter, C. 2016, A&ARv, 24, 10

Thater, S., Krajnović, D., Cappellari, M., et al. 2019, A&A, 625, A62
Thater, S., Krajnović, D., Weilbacher, P. M., et al. 2022, MNRAS, 509, 5416
van den Bosch, R. C. E. 2016, ApJ, 831, 134
Vanderbeke, J., Baes, M., Romanowsky, A. J., et al. 2011, MNRAS, 412, 2017
Veale, M., Ma, C.-P., Greene, J. E., et al. 2018, MNRAS, 473, 5446
Watson, L. C., Martini, P., Dasyra, K. M., et al. 2008, ApJ, 682, L21
White, R. L., & Becker, R. H. 1992, ApJS, 79, 331
Wójtowicz, A., Stawarz, Ł., Machalski, J., et al. 2021, ApJ, 922, 197
Wójtowicz, A., Stawarz, Ł., Cheung, C. C., et al. 2023, ApJ, 944, 195
Young, L. M. 2002, AJ, 124, 788
Young, L. M. 2005, ApJ, 634, 258
Young, L. M., Bureau, M., Davis, T. A., et al. 2011, MNRAS, 414, 940
Yu, Q. 2002, MNRAS, 331, 935
Yu, L.-M., Bian, W.-H., Wang, C., et al. 2019, MNRAS, 488, 1519

Appendix A: The sample

Table A.1. Radio and IR data for radio-detected early-type galaxies

Name (1)	RA [deg] (2)	DEC [deg] (3)	morph (4)	$F_{1.4}$ [mJy] (5)	F_3 [mJy] (6)	Dist [Mpc] (7)	M_{BH} [$M_\odot$] (8)	Ref. (9)	$log_{10}\sigma$ [km/s] (10)	Ref. (11)	$log_{10}\frac{L_{1.4}}{L_{Edd}}$ (12)	$log_{10}\frac{L_3}{L_{Edd}}$ (13)
0026+129	7.307083	13.267778	E	7.4±0.5[b]	1.2	406.2±40.62	$8.49^{+0.10}_{-0.12}$	[B18]	-		-7.28	-7.74
3C 120	68.29596	5.35428	L	3439±103.2[b]	2615.3	141.4±14.1	$7.73^{+0.15}_{-0.15}$	[B16]	2.21±0.05	[B16]	-4.77	-4.56
3C 390.3	280.537458	79.771424	E	11226±1122.6[a]	87.4	240.3±24	$8.62^{+0.16}_{-0.16}$	[B16]	2.44±0.03	[B16]	-4.68	-6.46
A 1836 BCG	210.424356	-11.607026	L	1870±39[f]	24.2	152.4±8.4	$9.57^{+0.06}_{-0.06}$	[B16]	2.46±0.02	[B16]	-6.81	-8.37
Ark120	79.04763	-0.15006	L	12.3±0.6[b]	1.8	140.1±14	$8.05^{+0.17}_{-0.17}$	[B16]	2.28±0.02	[B16]	-7.54	-8.05
Arp151	71.400697	54.382502	L	11.2±0.5[b]	0.4	90.3±9	$6.65^{+0.16}_{-0.16}$	[B16]	2.07±0.01	[B16]	-6.57	-7.68
Cygnus A	299.868153	40.733916	L	1598±41[d]	-	257.1±25.7	$9.41^{+0.13}_{-0.13}$	[B16]	2.43±0.02	[B16]	-6.26	-
ESO 444- G 025	201.027727	-31.670042	L	8.8±0.6[b]	1.1	149.4±14.94	$9.98^{+0.02}_{-0.02}$	[B21]	-		-9.56	-10.14
Holm 15A	10.460294	-9.303129	E	58.1±2.5[b]	6.6	163.9±16.39	$10.60^{+0.09}_{-0.09}$	[M19]	2.45±0.05	[V18]	-9.29	-9.90
IC1459	344.29446	-36.46194	E	1279.7±45.2[b]	317.5	28.9±3.7	$9.39^{+0.08}_{-0.08}$	[B16]	2.53±0.02	[B16]	-8.24	-8.51
Mrk0279	208.264362	69.308213	L	24±1.1[b]	3.9	130.4±13	$7.40^{+0.23}_{-0.23}$	[B16]	2.29±0.03	[B16]	-6.67	-7.12
Mrk0509	311.04033	-10.72306	L	18.6±1[b]	2.9	147.3±14.7	$8.03^{+0.15}_{-0.15}$	[B16]	2.26±0.03	[B16]	-7.30	-7.78
Mrk1216	127.196292	-6.940139	E	9.2±0.6[b]	2.5	94±9.4	$9.69^{+0.15}_{-0.15}$	[S19]	2.51±0.05	[S19]	-9.66	-9.89
Mrk1310	180.30982	-3.67808	E	3.4±0.5[b]	0.7	83.8±8.4	$6.19^{+0.19}_{-0.19}$	[B16]	1.92±0.03	[B16]	-6.69	-7.04
Mrk1383	217.27745	1.285132	E	3.6±0.6[b]	0.4	254.4±25.44	$8.65^{+0.13}_{-0.13}$	[Y19]	2.34±0.03	[W08]	-8.16	-8.78
Mrk0335	1.581339	20.202914	E	7.6±0.6[b]	1.9	76.9±7.69	$7.23^{+0.04}_{-0.04}$	[B18]	-		-7.45	-7.72
Mrk0771	188.01502	20.158114	L	3.1±0.5[b]	1.8	187.8±18.78	$8.09^{+0.37}_{-0.37}$	[Y19]	2.21±0.09	[D07]	-7.93	-7.83
NGC0193	9.827446	3.331117	E	983.1±31[b]	19.7	49.7±5	$8.40^{+0.32}_{-0.32}$	[B16]	2.27±0.04	[B16]	-6.89	-8.26
NGC0221	10.6743	40.865287	E	0.7±0.5[e]	-	0.8±0.01	$6.39^{+0.19}_{-0.19}$	[B16]	1.87±0.02	[B16]	-11.61	-
NGC0315	14.45368	30.352448	E	1800±100[e]	213.3	57.7±5.8	$8.92^{+0.31}_{-0.31}$	[B16]	2.49±0.04	[B16]	-7.02	-7.61
NGC0383	16.853995	32.412559	L	4800±200[e]	33.4	59.2±5.9	$8.76^{+0.32}_{-0.32}$	[B16]	2.38±0.03	[B16]	-6.41	-8.24
NGC0404	17.362587	35.718131	E	3.7±0.5[b]	0.6	3.1±0.3	$5.65^{+0.25}_{-0.25}$	[B16]	1.39±0.09	[B16]	-8.98	-9.43
NGC0524	21.19867	9.53936	L	3.1±0.4[b]	0.6	24.2±2.2	$8.94^{+0.05}_{-0.05}$	[B16]	2.37±0.02	[B16]	-10.56	-10.94
NGC0541	21.434617	-1.37958	E	538.2±11.9[f]	3.6	63.7±6.4	$8.59^{+0.34}_{-0.34}$	[B16]	2.28±0.01	[B16]	-7.13	-8.97
NGC0584	22.836458	-6.868056	E	0.6±0.5[e]	-	18.3±1.83	$8.13^{+0.17}_{-0.17}$	[T19]	2.28±0.01	[T19]	-10.70	-
NGC0741	29.087639	5.628938	E	1059±21[f]	4.9	65.7±6.6	$8.67^{+0.37}_{-0.37}$	[B16]	2.37±0.02	[B16]	-6.89	-8.89
NGC1023	40.100042	39.063285	L	0.6±0.1[g]	-	10.8±0.8	$7.62^{+0.05}_{-0.05}$	[B16]	2.22±0.02	[B16]	-10.68	-
NGC1052	40.26996	-8.25586	E	912.5±27.4[b]	376.4	18.1±1.8	$8.24^{+0.29}_{-0.29}$	[B16]	2.28±0.01	[B16]	-7.64	-7.69
NGC1194	45.954621	-1.103743	L	2.5±0.2[c]	0.6	58±6.3	$7.85^{+0.05}_{-0.05}$	[B16]	2.17±0.07	[B16]	-8.80	-9.09
NGC1275	49.950667	41.511696	E	22829.2±684.9[b]	9319.1	70±7	$8.98^{+0.20}_{-0.20}$	[B16]	2.39±0.05	[B16]	-5.81	-5.87
NGC1316	27.823171	34.848618	E	150000±10000[b]	19.6	18.6±0.6	$8.18^{+0.25}_{-0.25}$	[B16]	2.35±0.02	[B16]	-5.34	-8.89
NGC1332	51.571884	-21.335216	E	4.8±0.5[b]	0.9	22.3±1.9	$8.83^{+0.04}_{-0.04}$	[B16]	2.52±0.02	[B16]	-10.33	-10.72
NGC1358	53.41562	-5.08956	L	19.6±0.7[b]	1.1	48.2±4.8	$8.37^{+0.32}_{-0.32}$	[B16]	2.23±0.05	[B16]	-8.59	-9.51
NGC1380	54.114968	-34.976225	L	1.6±0.5[e]	0.7	18.7±1.87	$8.17^{+0.17}_{-0.17}$	[K22]	2.34±0.02	[V11]	-10.29	-10.33
NGC1399	54.62092	-35.45019	E	2200±100[e]	5.4	20.9±0.7	$8.94^{+0.31}_{-0.31}$	[B16]	2.53±0.02	[B16]	-7.83	-10.11
NGC1407	55.04971	-18.58028	E	87.7±3.5[b]	5.7	28±3.4	$9.65^{+0.08}_{-0.08}$	[B16]	2.45±0.02	[B16]	-9.69	-10.55
NGC1453	56.613542	-3.968778	E	28.1±1[b]	8	38.7±3.87	$9.46^{+0.06}_{-0.06}$	[L20]	2.43±0.05	[B16]	-9.71	-9.93
NGC1497	60.52846	23.13292	L	22.8±0.8[b]	12.9	75.3±7.5	$8.63^{+0.19}_{-0.19}$	[B16]	2.39±0.04	[B16]	-8.39	-8.31
NGC1550	64.90817	2.40992	E	16.6±1.6[b]	0.2	51.6±5.6	$9.57^{+0.07}_{-0.07}$	[B16]	2.48±0.02	[B16]	-9.80	-11.39
NGC1600	67.91583	-5.08678	E	61.6±2.6[b]	0.5	64±6.4	$10.23^{+0.04}_{-0.04}$	[B16]	2.47±0.02	[B16]	-9.70	-11.46
NGC2110	88.04725	-7.45628	E	298.8±9[b]	60.8	29.1±2.9	$8.12^{+0.64}_{-0.64}$	[B16]	2.30±0.05	[B16]	-7.59	-7.95
NGC2179	92.00933	-21.74714	L	13.8±0.7[b]	2.1	35.8±3.6	$8.31^{+0.23}_{-0.23}$	[B16]	2.19±0.03	[B16]	-8.94	-9.43
NGC2329	107.28262	48.61478	E	363.7±13.1[b]	52.5	72.3±7.2	$8.18^{+0.18}_{-0.18}$	[B16]	2.34±0.03	[B16]	-6.78	-7.29
NGC2685	133.894628	58.734398	L	1.9±0.5[e]	-	12.5±1.3	$6.59^{+0.41}_{-6.59}$	[B16]	2.02±0.02	[B16]	-8.99	-
NGC2693	134.246955	51.34744	E	8.5±0.9[b]	1.2	48±4.8	$9.23^{+0.10}_{-0.10}$	[P22]	2.54±0.06	[K01]	-9.81	-10.33
NGC2787	139.827486	69.203253	L	11.3±0.6[b]	4.7	7.4±1.2	$7.61^{+0.09}_{-0.09}$	[B16]	2.28±0.02	[B16]	-9.69	-9.74
NGC2892	143.220542	67.617389	E	236±23.6[c]	8.8	86.2±8.6	$8.43^{+0.11}_{-0.11}$	[B16]	2.47±0.03	[B16]	-7.06	-8.16
NGC2911	143.44212	10.15261	E	56.5±1.7[b]	23.1	43.5±4.3	$9.09^{+0.29}_{-0.29}$	[B16]	2.32±0.03	[B16]	-8.94	-8.99
NGC2974	145.63825	-3.69969	L	10.4±0.5[b]	2.6	21.5±2.4	$8.23^{+0.09}_{-0.09}$	[B16]	2.36±0.02	[B16]	-9.42	-9.70
NGC3078	149.60254	-26.92672	E	313.1±10.9[b]	47.9	32.8±3.3	$7.91^{+0.42}_{-0.42}$	[B16]	2.32±0.03	[B16]	-7.26	-7.74
NGC3091	150.059543	-19.636961	E	2.5±0.5[e]	0.4	51.2±8.3	$9.56^{+0.07}_{-0.07}$	[B16]	2.49±0.02	[B16]	-10.62	-11.08
NGC3115	151.30825	-7.718583	L	0.6±0.5[e]	-	9.5±0.4	$8.95^{+0.09}_{-0.09}$	[B16]	2.36±0.02	[B16]	-12.09	-
NGC3245	156.82575	28.50756	E	6.7±0.5[e]	1.6	21.4±2	$8.38^{+0.11}_{-0.11}$	[B16]	2.25±0.02	[B16]	-9.77	-10.06
NGC3379	161.956616	12.581624	E	2.7±0.5[b]	0.3	10.7±0.5	$8.62^{+0.11}_{-0.11}$	[B16]	2.27±0.02	[B16]	-11.01	-11.63
NGC3414	162.81825	27.97492	L	4.4±0.4[e]	1.6	25.2±2.7	$8.40^{+0.07}_{-0.07}$	[B16]	2.28±0.02	[B16]	-9.83	-9.94
NGC3489	165.077375	13.901222	L	1.5±0.5[e]	-	12.1±0.8	$6.78^{+0.05}_{-0.05}$	[B16]	2.01±0.02	[B16]	-9.31	-
NGC3516	166.69879	72.56953	L	31.3±1.3[b]	2.1	37.9±3.8	$7.37^{+0.16}_{-0.16}$	[B16]	2.26±0.01	[B16]	-7.59	-8.44

Table A.1. continued.

Name (1)	RA [deg] (2)	DEC [deg] (3)	morph (4)	$F_{1.4}$ [mJy] (5)	F_3 [mJy] (6)	Dist [Mpc] (7)	M_{BH} $[M_{\odot}]$ (8)	Ref. (9)	$log_{10}\sigma$ [km/s] (10)	Ref. (11)	$log_{10}\frac{L_{1.4}}{L_{Edd}}$ (12)	$log_{10}\frac{L_3}{L_{Edd}}$ (13)
NGC3557	167.490175	-37.539155	E	790±60^{e}	9.7	30.7±3.07	$8.85^{+0.02}_{-0.02}$	[R19]	2.45±0.03	[B07]	-7.85	-9.43
NGC3585	168.321214	-26.75484	E	0.6±0.5^{e}	-	20.5±1.7	$8.52^{+0.13}_{-0.13}$	[B16]	2.33±0.02	[B16]	-10.99	-
NGC3607	169.22775	18.05125	E	6.9±0.4^{b}	1.3	22.6±1.8	$8.14^{+0.16}_{-0.16}$	[B16]	2.32±0.02	[B16]	-9.47	-9.86
NGC3608	169.245632	18.148684	E	1.3±0.5^{e}	-	22.8±1.5	$8.67^{+0.10}_{-0.10}$	[B16]	2.23±0.02	[B16]	-10.72	-
NGC3640	170.278542	3.234833	L	42±2^{e}	-	13±1.3	$8.89^{+0.02}_{-0.02}$	[T19]	2.25±0.02	[T19]	-9.92	-
NGC3665	171.18212	38.76281	E	112.2±3.7^{b}	3.8	34.7±6.7	$8.76^{+0.09}_{-0.09}$	[B16]	2.34±0.02	[B16]	-8.51	-9.64
NGC3706	172.435125	-36.391306	L	53±2^{e}	0.9	46±4.6	$9.77^{+0.06}_{-0.06}$	[B16]	2.51±0.01	[B16]	-9.60	-11.04
NGC3801	175.07096	17.7275	L	1143.3±38.5^{f}	7	46.3±4.6	$8.28^{+0.31}_{-0.31}$	[B16]	2.32±0.04	[B16]	-6.77	-8.65
NGC3842	176.008958	19.949806	E	12.6±0.6^{b}	0.5	92.2±10.6	$9.96^{+0.14}_{-0.14}$	[B16]	2.44±0.02	[B16]	-9.81	-10.88
NGC3862	176.270871	19.606317	E	5689±131^{f}	139	84.6±8.5	$8.41^{+0.37}_{-0.37}$	[B16]	2.32±0.03	[B16]	-5.68	-6.96
NGC3923	177.757059	-28.806017	E	1±0.5^{e}	-	20.9±2.7	$9.45^{+0.12}_{-0.12}$	[B16]	2.35±0.02	[B16]	-11.69	-
NGC3945	178.307208	60.675556	L	1.6±0.5^{e}	1.1	19.5±2	$6.94^{+0.46}_{-6.94}$	[B16]	2.25±0.02	[B16]	-9.03	-8.86
NGC3998	179.48392	55.4535	E	98.4±3^{b}	33.3	14.3±1.3	$8.93^{+0.05}_{-0.05}$	[B16]	2.35±0.02	[B16]	-9.50	-9.64
NGC4026	179.854958	50.961694	L	1.3±0.5^{e}	-	13.4±1.7	$8.26^{+0.12}_{-0.12}$	[B16]	2.19±0.02	[B16]	-10.77	-
NGC4036	180.35925	61.89569	L	11.6±0.5^{b}	2.2	19±1.9	$7.89^{+0.36}_{-0.36}$	[B16]	2.26±0.02	[B16]	-9.14	-9.54
NGC4143	182.40158	42.5335	L	9.9±0.9^{b}	1.4	14.8±1.5	$7.92^{+0.36}_{-0.36}$	[B16]	2.25±0.02	[B16]	-9.46	-9.98
NGC4150	182.640247	30.401615	E	1.2±0.5^{e}	-	12.8±1.3	$5.94^{+0.44}_{-5.94}$	[B16]	1.91±0.02	[B16]	-8.52	-
NGC4151	182.6355	39.40581	L	359.6±10.8	70.9	20±2.8	$7.81^{+0.08}_{-0.08}$	[B16]	1.98±0.01	[B16]	-7.53	-7.90
NGC4203	183.77179	33.19797	L	6.1±0.5^{b}	2.7	14.1±1.4	$7.82^{+0.26}_{-0.26}$	[B16]	2.11±0.02	[B16]	-9.61	-9.64
NGC4261	184.846752	5.825215	E	22000±1000^{e}	111.4	32.4±2.8	$8.72^{+0.10}_{-0.10}$	[B16]	2.42±0.02	[B16]	-6.23	-8.20
NGC4278	185.02821	29.28081	E	385±11.6^{b}	105.5	15±1.5	$7.96^{+0.27}_{-0.27}$	[B16]	2.33±0.02	[B16]	-7.90	-8.13
NGC4281	185.089684	5.386392	L	0.8±0.5^{e}	-	26.7±1.5	$8.73^{+0.08}_{-0.08}$	[T19]	2.36±0.02	[T19]	-10.85	-
NGC4335	185.7585	58.44464	E	121.3±4.5^{b}	8.6	59.1±5.9	$8.39^{+0.31}_{-0.31}$	[B16]	2.41±0.01	[B16]	-7.64	-8.46
NGC4374	186.265597	12.886983	E	7000±600^{e}	52.8	10.2±1.02	$8.97^{+0.05}_{-0.05}$	[S16]	2.47±0.02	[S16]	-7.98	-9.78
NGC4382	186.350451	18.191487	E	0.7±0.5^{e}	-	17.9±1.8	$7.11^{+1.24}_{-7.11}$	[B16]	2.25±0.02	[B16]	-9.64	-
NGC4429	186.86045	11.10771	L	1.1±0.1^{g}	0.3	18.2±1.8	$7.85^{+0.35}_{-0.35}$	[B16]	2.25±0.02	[B16]	-10.16	-10.40
NGC4459	187.250037	13.978373	E	1.4±0.1^{g}	0.4	16±0.5	$7.84^{+0.09}_{-0.09}$	[B16]	2.20±0.02	[B16]	-10.16	-10.37
NGC4472	187.44417	8.00081	E	219.9±7.8^{b}	22.5	17.1±0.6	$9.4^{+0.04}_{-0.04}$	[B16]	2.40±0.02	[B16]	-9.47	-10.13
NGC4477	187.509159	13.636604	L	0.8±0.5^{e}	-	20.8±2.1	$7.55^{+0.30}_{-0.30}$	[B16]	2.17±0.02	[B16]	-9.89	-
NGC4486	187.70593	12.391123	E	210000±10000^{e}	1062.3	16.7±0.6	$9.58^{+0.10}_{-0.10}$	[B16]	2.42±0.02	[B16]	-6.69	-8.65
NGC4526	188.51158	7.69944	L	12±0.5^{b}	-	16.4±1.8	$8.65^{+0.12}_{-0.12}$	[B16]	2.32±0.02	[B16]	-10.02	-
NGC4546	188.872958	-3.793194	E	11±0.6^{b}	4.2	10.6±1.06	$8.41^{+0.03}_{-0.03}$	[R20]	2.40±0.02	[R16]	-10.19	-10.28
NGC4552	188.91575	12.55617	E	100.1±3^{b}	26	15.3±1	$8.70^{+0.05}_{-0.05}$	[B16]	2.35±0.02	[B16]	-9.21	-9.46
NGC4564	189.112428	11.439283	E	1.6±0.5^{e}	-	15.9±0.5	$7.95^{+0.12}_{-0.12}$	[B16]	2.19±0.02	[B16]	-10.22	-
NGC4596	189.98311	10.17614	L	0.8±0.5^{e}	-	16.5±6.2	$7.89^{+0.26}_{-0.26}$	[B16]	2.10±0.02	[B16]	-10.43	-
NGC4636	190.707615	2.687776	E	78.7±2.9^{b}	3.4	13.7±1.4	$8.58^{+0.22}_{-0.22}$	[B16]	2.26±0.02	[B16]	-9.29	-10.32
NGC4649	190.91721	11.55261	E	29.1±1.3^{b}	6.6	16.5±0.6	$9.67^{+0.10}_{-0.10}$	[B16]	2.43±0.02	[B16]	-10.65	-10.96
NGC4697	192.149491	-5.800742	L	0.6±0.5^{e}	1.4	12.5±0.4	$8.31^{+0.11}_{-0.11}$	[B16]	2.23±0.02	[B16]	-11.21	-10.52
NGC4786	193.635083	-6.859417	E	9.2±0.5^{e}	0.9	55.7±5.57	$8.70^{+0.33}_{-0.31}$	[K24]	2.45±0.04	[B16]	-9.12	-9.80
NGC4889	195.033875	27.977	E	1.2±0.5^{e}	0.3	102±5.2	$10.32^{+0.44}_{-0.44}$	[B16]	2.56±0.02	[B16]	-11.10	-11.37
NGC5018	198.254305	-19.518193	L	2±0.5^{e}	0.3	40.5±4.9	$8.02^{+0.08}_{-0.08}$	[B16]	2.32±0.01	[B16]	-9.38	-9.87
NGC5044	198.849875	-16.385528	E	36.1±1.5^{b}	8.4	27.8±2.78	$9.28^{+0.01}_{-0.01}$	[D17]	2.48±0.02	[D17]	-9.71	-10.01
NGC5077	199.88196	-12.65692	E	156.7±4.7^{b}	107	38.7±8.4	$8.93^{+0.27}_{-0.27}$	[B16]	2.35±0.02	[B16]	-8.44	-8.27
NGC5102	200.490029	-36.630244	L	1.7±0.5^{e}	-	4.7±0.47	$5.94^{+0.38}_{-0.38}$	[S19]	1.79±0.05	[S19]	-9.25	-
NGC5127	200.937583	31.56575	E	1980±198^{c}	4	62.5±6.3	$8.27^{+0.41}_{-0.41}$	[B16]	2.29±0.11	[B16]	-6.26	-8.62
NGC5128	201.365063	-43.019113	L	1330000±13300^{0}	-	3.6±0.2	$7.76^{+0.08}_{-0.08}$	[B16]	2.18±0.02	[B16]	-5.40	-
NGC5252	204.566	4.54364	L	16.3±0.6^{b}	3.9	103.7±10.4	$9.07^{+0.34}_{-0.34}$	[B16]	2.28±0.02	[B16]	-8.70	-8.99
NGC5273	205.53474	35.654214	E	3.5±0.4^{e}	0.6	15.5±1.5	$6.61^{+0.27}_{-0.27}$	[B16]	1.82±0.02	[B16]	-8.56	-9.00
NGC5283	205.273995	67.672311	L	13.4±0.6^{b}	2.6	34.5±3.5	$7.41^{+0.33}_{-0.33}$	[B16]	2.13±0.04	[B16]	-8.08	-8.46
NGC5328	208.222138	-28.489402	E	0.9±0.5^{e}	-	64.1±7	$9.67^{+0.16}_{-0.16}$	[B16]	2.52±0.02	[B16]	-10.98	-
NGC5419	210.91129	-33.97969	E	790±60^{e}	21.7	56.2±6.1	$9.86^{+0.14}_{-0.14}$	[B16]	2.57±0.01	[B16]	-8.34	-9.57
NGC5490	212.48908	17.54558	E	1300±100^{e}	21.8	65.2±6.5	$8.73^{+0.35}_{-0.35}$	[B16]	2.41±0.04	[B16]	-6.86	-8.31
NGC5813	225.296796	1.701981	E	15.8±1.1^{b}	1.2	19.7±1.97	$8.85^{+0.06}_{-0.06}$	[S16]	2.36±0.02	[S16]	-9.94	-10.73
NGC5846	226.62217	1.60528	E	21±1.3^{b}	48.7	24.9±2.3	$9.04^{+0.06}_{-0.06}$	[B16]	2.35±0.02	[B16]	-9.80	-9.11
NGC6086	243.148053	29.484791	E	100±1.4^{e}	-	138±11.5	$9.57^{+0.17}_{-0.17}$	[B16]	2.50±0.02	[B16]	-8.17	-
NGC6251	248.133208	82.537889	E	1800±100^{e}	174.8	108.4±9	$8.79^{+0.16}_{-0.16}$	[B16]	2.46±0.02	[B16]	-6.34	-7.02
NGC6958	312.177458	-37.997417	L	16.3±1^{b}	2.1	27.1±2.71	$8.56^{+0.33}_{-0.29}$	[T22]	2.23±0.01	[T22]	-9.36	-9.92
NGC7052	319.637708	26.447028	E	162.1±5.3^{b}	17.6	70.4±8.4	$8.60^{+0.23}_{-0.23}$	[B16]	2.42±0.02	[B16]	-7.57	-8.20
NGC7332	339.35225	23.798333	L	0.6±0.5^{e}	-	21.7±2.2	$7.08^{+0.18}_{-0.18}$	[B16]	2.10±0.02	[B16]	-9.51	-
NGC7619	350.06092	8.20633	E	20.3±1.1^{b}	4.7	51.5±7.4	$9.40^{+0.11}_{-0.11}$	[B18]	2.51±0.02	[B16]	-9.55	-9.85
NGC7626	350.177275	8.216967	E	842±15^{f}	10.4	38.1±3.8	$8.58^{+0.33}_{-0.33}$	[B16]	2.37±0.02	[B16]	-7.37	-8.95

Table A.1. continued.

Name (1)	RA [deg] (2)	DEC [deg] (3)	morph (4)	$F_{1.4}$ [mJy] (5)	F_3 [mJy] (6)	Dist [Mpc] (7)	M_{BH} [$M_\odot$] (8)	Ref. (9)	$log_{10}\sigma$ [km/s] (10)	Ref. (11)	$log_{10}\frac{L_{1.4}}{L_{Edd}}$ (12)	$log_{10}\frac{L_3}{L_{Edd}}$ (13)
UGC12064	337.83575	39.358194	L	3800±380^c	9.7	34.7±6.7	$8.84^{+0.52}_{-0.52}$	[B16]	2.41±0.03	[B16]	-7.06	-9.32
UGC1214	25.99042	2.34975	L	24±1.1^b	2.9	59.9±6	$7.74^{+0.18}_{-7.74}$	[B16]	2.02±0.06	[B16]	-7.68	-8.27
UGC1841	35.797547	42.992051	E	8200±820^c	82.9	74.9±7.5	$8.47^{+0.19}_{-0.19}$	[B16]	2.47±0.04	[B16]	-5.68	-7.35
UGC7115	182.0245	25.23672	E	87.3±2.7^b	17.7	88.2±8.8	$9.00^{+0.45}_{-0.45}$	[B16]	2.25±0.08	[B16]	-8.04	-8.41
UGC9799	229.18575	7.02169	E	5499.3±209.1^b	167.8	151.1±15.1	$8.89^{+0.8}_{-8.89}$	[B16]	2.37±0.02	[B16]	-5.67	-6.85

Notes. Column 1: Source name. Columns 2 and 3: RA and DEC J2000, in units of degrees. Column 4: Host galaxy optical morphology: E– elliptical, L– lenticular. Column 5: 1.4 GHz radio flux, in mJy, References:[0] Cooper et al. (1965); [a] White & Becker (1992); [b] Condon et al. (1998); [c] Condon et al. (2002); [d] Bîrzan et al. (2004); [e] Brown et al. (2011); [f] Allison et al. (2014); [g] Nyland et al. (2017). Column 6: 3 GHz core radio flux, in mJy, measured at the position of the optical core. Column 7: Reported distance in Mpc. Column 8: Logarithm of Black Hole Mass in $M_\odot$. Column 9: References for Column 8: [B16]– van den Bosch (2016); [S16]–;Saglia et al. (2016);[D17]–Diniz et al. (2017);[B18]–Bentz & Manne-Nicholas (2018); [M19]–Mehrgan et al. (2019);[S19]–Sahu et al. (2019b); [T19]–Thater et al. (2019);[Y19]–Yu et al. (2019);[L20]–Liepold et al. (2020);[R20]–Ricci & Steiner (2020);[B21]–den Brok et al. (2021);[K22]–Kabasares et al. (2022) ; [P22]–Pilawa et al. (2022);[T22]–Thater et al. (2022). Column 10: Stellar velocity dispersion, in km/s, measured in host galaxy effective radius R_{eff}. Column 11: References for Column 10: [K01]– Kuntschner et al. (2001);[B07]–Brough et al. (2007);[D07]– Dasyra et al. (2007);[W08]–Watson et al. (2008); [V11]–Vanderbeke et al. (2011);[B16]–van den Bosch (2016) ;[R16]–Ricci et al. (2016);[S16]–Saglia et al. (2016);[D17]–Diniz et al. (2017);[V18]–Veale et al. (2018);[T19]–Thater et al. (2019); [S19]–Sahu et al. (2019b);[T22]–Thater et al. (2022). Column 12: Fraction of total 1.4 GHz radio luminosity to Eddington luminosity. Column 13: Fraction of measured core-related 3 GHz radio luminosity to Eddington luminosity.

Appendix B: WISE data

Table B.1. WISE colors of radio-bright (left) and radio-dim objects (right) based on magnitudes measured with profile-fitting photometry in the WISE All-Sky Survey catalog.

radio-bright galaxies			radio-dim galaxies		
Name (1)	W1-W2 [mag] (2)	W2-W3 [mag] (3)	Name (1)	W1-W2 [mag] (2)	W2-W3 [mag] (3)
PG 0026+129	0.966	2.377	ESO 444-G25	-0.074	0.571
3C 120	1.014	2.921	Holm15A	-0.045	0.652
3C 390.3	1.037	2.607	MRK 1216	-0.062	0.692
A1836BCG	-0.072	0.745	NGC 0221	-0.642	0.268
Ark120	0.887	2.371	NGC 0404	0.056	2.479
Cygnus A	0.933	4.428	NGC 0524	0.004	1.435
IC 1459	-0.02	0.847	NGC 0584	0.001	0.564
MRK 0279	0.926	3.537	NGC 1023	-0.048	0.524
MRK 0509	0.89	2.671	NGC 1194	1.307	2.975
MRK 1310	0.596	3.017	NGC 1332	-0.025	0.995
MRK 1383	0.942	2.822	NGC 1358	-0.005	1.671
MRK 335	0.981	2.384	NGC 1380	0.016	1.44
MRK 771	0.99	3.058	NGC 1399	-0.222	0.662
NGC 0193	-0.08	0.922	NGC 1407	-0.032	0.538
NGC 0315	0.039	1.906	NGC 1453	0.002	0.508
NGC 0383	0.027	1.653	NGC 1497	0.208	2.397
NGC 0541	-0.058	1.031	NGC 1550	-0.067	0.586
NGC 0741	-0.021	0.45	NGC 1600	-0.028	0.444
NGC 1052	0.196	2.542	NGC 2179	-0.024	1.784
NGC 1275	1.006	4.005	NGC 2693	-0.011	1.127
NGC 2110	0.781	2.625	NGC 2787	-0.008	1.322
NGC 2329	0.006	1.03	NGC 2911	-0.021	1.524
NGC 2892	-0.026	0.591	NGC 2974	-0.019	1.246
NGC 3078	0.021	0.836	NGC 3091	-0.031	0.536
NGC 3557	-0.015	0.691	NGC 3115	-0.725	0.686
NGC 3801	-0.032	1.882	NGC 3245	0.011	1.978
NGC 3862	0.06	1.422	NGC 3379	-0.355	0.541
NGC 4151	0.818	2.719	NGC 3414	-0.036	0.977
NGC 4261	-0.03	1.055	NGC 3489	0.043	1.402
NGC 4278	0.002	0.962	NGC 3585	-0.008	0.735
NGC 4335	-0.032	1.447	NGC 3607	0.037	1.746
NGC 4374	0.016	0.85	NGC 3608	-0.024	0.517
NGC 4486	0.078	1.184	NGC 3640	-0.018	0.495
NGC 5127	-0.051	0.941	NGC 3665	0.064	2.599
NGC 5128	0.505	2.136	NGC 3706	-0.013	0.567
NGC 5283	0.12	2.307	NGC 3842	-0.046	0.449
NGC 5490	-0.043	0.546	NGC 3923	0.014	0.577
NGC 6086	-0.06	0.511	NGC 3998	0.062	1.844
NGC 6251	0.148	2.054	NGC 4026	-0.017	0.49
NGC 7052	-0.01	1.536	NGC 4036	0.013	1.093
NGC 7626	-0.01	0.516	NGC 4143	-0.024	1.101
UGC 12064	-0.05	1.392	NGC 4203	0.044	1.442
UGC 1841	-0.011	0.952	NGC 4281	0.009	1.719
UGC 7115	-0.058	0.882	NGC 4429	0.059	2.022
			NGC 4459	0.043	2.085
			NGC 4472	-0.366	0.601
			NGC 4477	-0.021	0.891
			NGC 4526	0.075	2.264
			NGC 4546	-0.032	0.797
			NGC 4552	-0.026	0.677
			NGC 4564	-0.043	0.562
			NGC 4596	-0.032	1.495
			NGC 4636	-0.025	0.585
			NGC 4649	-0.491	0.675
			NGC 4697	-0.008	0.921
			NGC 4889	-0.055	0.498
			NGC 5018	0.05	1.294
			NGC 5044	-0.025	0.83
			NGC 5077	-0.044	0.779
			NGC 5102	0.085	1.003
			NGC 5252	0.829	2.018
			NGC 5273	0.172	2.547
			NGC 5328	-0.044	0.529
			NGC 5813	0.004	0.414
			NGC 5846	-0.031	0.558
			NGC 6958	0.021	1.552
			NGC 7332	-0.047	0.659
			NGC 7619	-0.023	0.508

Appendix C: FIR data

Table C.1. Information on the measured FIR fluxes for all sources observed by the IRAS satellite.

Name (1)	$F_{60\mu m}$ [Jy] (2)	$err\_F_{60\mu m}$ [Jy] (3)	$F_{100\mu m}$ [Jy] (4)	$err\_F_{100\mu m}$ [Jy] (5)	FIR [10^{-14} W m^{-2}] (6)	err_FIR [10^{-14} W m^{-2}] (7)	q - (8)	err_q - (9)
3C 120	1.32	0.09	2.64	0.18	7.56	0.38	-0.23	0.03
Ark 120	0.66	0.07	1.30	0.14	3.74	0.28	1.91	0.04
MRK 0279	1.08	0.17	2.28	0.18	6.33	0.61	1.85	0.05
MRK 0509	1.42	0.11	1.43	0.20	6.37	0.45	1.96	0.04
NGC 0383	0.44	0.05	1.20	0.20	2.93	0.31	-0.79	0.05
NGC 0404	2.27	0.27	4.78	0.53	13.30	1.11	2.98	0.07
NGC 0524	0.79	0.08	1.74	0.23	4.71	0.38	2.61	0.07
NGC 0741[a]	0.19	0.02	1.13	0.11	2.03	0.16	-0.29	0.03
NGC 1052	0.94	0.08	1.22	0.13	4.55	0.3	0.12	0.03
NGC 1275	7.22	0.65	8.01	0.72	33.3	2.3	-0.41	0.03
NGC 1316[a]	3.07	0.03	8.11	1.90	20.04	2.4	2.02	0.32
NGC 1332	0.52	0.04	1.80	0.13	3.92	0.21	2.34	0.05
NGC 1358[a]	0.38	0.05	0.93	0.20	2.38	0.29	1.51	0.06
NGC 1380	1.05	0.07	2.96	0.24	7.09	0.38	3.07	0.14
NGC 1407[a]	0.14	0.03	0.48	0.07	1.05	0.13	0.50	0.06
NGC 1600[a]	0.10	0.03	0.19	0.07	0.56	0.13	0.38	0.10
NGC 2110	4.46	0.4	6.26	0.69	22.21	1.57	1.30	0.03
NGC 2693	0.25	0.02	0.52	0.05	1.45	0.09	1.66	0.05
NGC 2974	0.48	0.05	1.60	0.29	3.54	0.4	1.96	0.05
NGC 3245	2.03	0.18	3.37	0.30	10.76	0.71	2.63	0.04
NGC 3516	1.74	0.12	2.17	0.13	8.32	0.43	1.85	0.03
NGC 3557[a]	0.24	0.05	0.75	0.17	1.71	0.26	-0.24	0.07
NGC 3665	2.00	0.24	6.37	0.64	14.41	1.12	1.53	0.04
NGC 3706[a]	0.07	0.05	0.22	0.08	0.50	0.18	0.40	0.16
NGC 3801[a]	0.17	0.05	2.80	0.09	4.05	0.20	-0.02	0.03
NGC 3842[a]	0.36	0.06	1.49	0.19	3.02	0.30	1.81	0.05
NGC 3998	0.44	0.05	0.93	0.16	2.58	0.25	0.84	0.04
NGC 4026[a]	0.1	0.03	0.56	0.13	1.02	0.18	2.32	0.18
NGC 4203	0.64	0.06	2.11	0.21	4.70	0.34	2.31	0.05
NGC 4261[a]	0.08	0.04	0.15	0.05	0.45	0.13	-2.27	0.13
NGC 4278	0.57	0.07	1.62	0.16	3.85	0.30	0.43	0.04
NGC 4281	0.59	0.07	1.55	0.53	3.85	0.70	3.11	0.28
NGC 4429	1.54	0.18	4.62	0.55	10.74	0.92	3.41	0.05
NGC 4459	1.75	0.21	4.34	0.52	11.07	0.95	3.33	0.04
NGC 4477	0.54	0.06	1.18	0.19	3.21	0.32	3.03	0.27
NGC 4526	5.93	0.71	16.00	2.24	39.12	3.65	2.94	0.04
NGC 4546[a]	0.26	0.05	0.89	0.22	1.95	0.31	1.67	0.07
NGC 4552[a]	0.16	0.05	0.53	0.06	1.18	0.17	0.50	0.06
NGC 4596	0.49	0.09	1.28	0.18	3.17	0.36	3.02	0.28
NGC 4649[a]	0.78	0.03	1.09	0.07	3.88	0.14	1.55	0.02
NGC 4697[a]	0.46	0.02	1.24	0.08	3.03	0.12	3.13	0.36
NGC 4786[b]	0.28	0.05	0.73	0.17	1.83	0.26	1.72	0.07
NGC 5018	1.01	0.11	1.90	0.19	5.63	0.43	2.88	0.11
NGC 5044[a]	0.14	0.06	0.15	0.07	0.64	0.20	0.67	0.14
NGC 5102	0.83	0.07	2.65	0.21	5.99	0.36	2.97	0.13
NGC 5128	172.00	15.48	338.00	27.04	977.20	60.77	0.80	0.05
NGC 5273[a]	0.90	0.04	1.56	0.12	4.85	0.19	2.57	0.05
NGC 5283[b]	0.13	0.03	0.75	0.14	1.36	0.20	1.43	0.07
NGC 6958	1.06	0.10	2.45	0.25	6.48	0.44	2.03	0.04
NGC 7052	0.45	0.04	1.48	0.12	3.29	0.21	0.73	0.03
NGC 7332[a]	0.21	0.03	0.41	0.11	1.19	0.17	2.72	0.37

Notes. Column 1: Object name and references to the provided fluxes if not cataloged in IRAS Source catalogs: [a]– Knapp et al. (1989); [b]– Moshir et al. (2008). Column 2: 60μm IRAS flux;
Column 4–100μm IRAS flux. Column 6: FIR flux calculated with the formula $F_{\rm FIR}/{\rm W\,m^{-2}} = 1.26\times10^{-14}\,[2.58\times S_{60\mu{\rm m}}/{\rm Jy} + S_{100\mu{\rm m}}/{\rm Jy}]$. Column 8: Fraction on FIR to 1.4 GHz radio flux, Columns 3, 5, 7, and 9: Errors corresponding to Columns 2, 4, 6, and 8, respectively.

Table C.2. Information on the FIR fluxes for sources with only upper limit estimates measured by the IRAS satellite.

Name (1)	$F_{60\mu m}$ [Jy] (2)	$err\_F_{60\mu m}$ [Jy] (3)	$F_{100\mu m}$ [Jy] (4)	$err\_F_{100\mu m}$ [Jy] (5)	FIR $[10^{-14}\,\mathrm{W\,m^{-2}}]$ (6)	err_FIR $[10^{-14}\,\mathrm{W\,m^{-2}}]$ (7)	q - (8)	err_q - (9)
PG 0026+129[d]	<0.03	-	<0.08	-	<0.19	-	<0.83	-
3C 390.3	<0.4	-	<1	-	<2.54	-	< 1.22	-
Cygnus A	2.33	0.16	<8.28	-	<17.86	-	<0.47	-
IC 1459	0.42	0.07	<1.04	-	<2.66	-	< -0.26	-
MRK 1383	0.24	0.04	0.38	0.09	1.23	0.17	1.96	0.09
MRK 335	0.45	0.05	<1	-	<2.71	-	<1.98	-
NGC 0584[c]	<0.04	-	0.59	0.1	0.87	0.13	<2.59	-
MRK 771[d]	0.16	0.04	<0.46	-	<1.1	-	<1.98	-
NGC 0221	<0.17	-	<0.63	-	<1.35	-	<2.71	-
NGC 0315	0.27	0.05	0.71	0.19	1.75	0.29	-0.22	0.07
NGC 0541[c]	<0.05	-	<0.13	-	<0.32	-	< -0.25	-
NGC 1023	0.18	0.04	0.52	0.12	1.25	0.21	2.77	0.11
NGC 1194	0.79	0.06	<1	-	<3.79	-	<2.61	-
NGC 1399[c]	<0.03	-	0.3	0.08	0.48	0.1	<-0.21	-
NGC 1453[c]	<0.04	-	0.75	0.13	1.06	0.16	<1	-
NGC 1550[c]	<0.03	-	<0.25	-	<0.39	-	<0.8	-
NGC 2329[c]	<0.03	-	<0.19	-	<0.35	-	< -0.6	-
NGC 2787	0.66	0.07	<2.05	-	<4.68	-	<2.04	-
NGC 2911	0.22	0.04	0.81	0.19	1.72	0.28	0.91	0.07
NGC 3115[c]	0.13	0.04	<0.11	-	<0.56	-	<2.4	-
NGC 3379[c]	<0.04	-	<0.11	-	<0.27	-	<1.42	-
NGC 3414	0.19	0.04	0.91	0.21	1.76	0.29	2.03	0.08
NGC 3585[c]	0.16	0.04	<0.09	-	<0.63	-	<2.44	-
NGC 3640[c]	<0.04	-	<0.07	-	<0.21	-	<0.12	-
NGC 3862[c]	0.21	0.05	<0.18	-	<0.9	-	< -1.37	-
NGC 3923[c]	<0.04	-	<0.14	-	<0.28	-	<1.88	-
NGC 4036	0.54	0.05	<1.6	-	<3.75	-	<1.94	-
NGC 4151	<6.64	-	<8.73	-	<32.33	-	<1.38	-
NGC 4335	0.27	0.04	1.09	0.24	2.22	0.33	0.69	0.07
NGC 4374	0.51	0.05	<1.41	-	<3.39	-	< -0.89	-
NGC 4472[a]	<0.19	-	<0.48	-	<1.21	-	<0.17	-
NGC 4486	0.39	0.05	1.02	0.3	2.55	0.41	-2.49	0.07
NGC 4564[c]	<0.06	-	<0.19	-	<0.43	-	<1.86	-
NGC 4636[c]	0.14	0.04	<0.07	-	<0.54	-	<0.26	-
NGC 4889[c]	<0.05	-	<0.07	-	<0.26	-	<1.76	-
NGC 5127[c]	<0.03	-	<0.06	-	<0.18	-	< -1.61	-
NGC 5328[c]	<0.03	-	<0.07	-	<0.19	-	<1.76	-
NGC 5419[c]	<0.04	-	0.23	0.07	0.41	0.08	<-0.51	-
NGC 5490[c]	<0.03	-	<0.19	-	<0.35	-	< -0.35	-
NGC 5813[c]	<0.02	-	<0.1	-	<0.2	-	< 0.53	-
NGC 5846[c]	<0.04	-	<0.13	-	<0.27	-	<0.54	-
NGC 6086[c]	<0.05	-	<0.19	-	<0.39	-	<0.01	-
NGC 6251[c]	<0.02	-	<0.11	-	<0.21	-	< -1.51	-
NGC 7619[c]	<0.04	-	<0.23	-	<0.41	-	<0.73	-
NGC 7626[c]	<0.04	-	<0.13	-	<0.29	-	< -1.03	-
UGC 1841[b]	<0.13	-	<0.35	-	<0.86	-	< -1.55	-

Notes. Column 1: Object name and references to the provided fluxes if not cataloged in the IRAS Source catalogs: [a]–Rice et al. (1988); [b]– Golombek et al. (1988); [c]– Knapp et al. (1989); [d]– Sanders et al. (1989). Column 2: 60μm IRAS flux. Column 4: 100μm IRAS flux. Column 6: FIR flux calculated with the formula $F_{\mathrm{FIR}}/\mathrm{W\,m^{-2}} = 1.26 \times 10^{-14}\,[2.58 \times S_{60\mu\mathrm{m}}/\mathrm{Jy} + S_{100\mu\mathrm{m}}/\mathrm{Jy}]$. Column 8: Fraction on FIR to 1.4 GHz radio flux. Columns 3, 5, 7, and 9: Errors corresponding to Columns 2, 4, 6, and 8, respectively.